JOURNAL OF GEOPHYSICAL RESEARCH, VOL. 108, NO. B5, 2236, doi:10.1029/2001JB000707, 2003

Tsunamis generated by subaerial mass flows

Joseph S. Walder
U.S. Geological Survey, Cascades Volcano Observatory, Vancouver, Washington, USA

Philip Watts
Applied Fluids Engineering, Inc., Long Beach, California, USA

Oscar E. Sorensen[1] and Kenneth Janssen
U.S. Geological Survey, Cascades Volcano Observatory, Vancouver, Washington, USA

Received 22 June 2001; revised 8 November 2002; accepted 20 December 2002; published 8 May 2003.

[1] Tsunamis generated in lakes and reservoirs by subaerial mass flows pose distinctive problems for hazards assessment because the domain of interest is commonly the "near field," beyond the zone of complex splashing but close enough to the source that wave propagation effects are not predominant. Scaling analysis of the equations governing water wave propagation shows that near-field wave amplitude and wavelength should depend on certain measures of mass flow dynamics and volume. The scaling analysis motivates a successful collapse (in dimensionless space) of data from two distinct sets of experiments with solid block "wave makers." To first order, wave amplitude/water depth is a simple function of the ratio of dimensionless wave maker travel time to dimensionless wave maker volume per unit width. Wave amplitude data from previous laboratory investigations with both rigid and deformable wave makers follow the same trend in dimensionless parameter space as our own data. The characteristic wavelength/water depth for all our experiments is simply proportional to dimensionless wave maker travel time, which is itself given approximately by a simple function of wave maker length/water depth. Wave maker shape and rigidity do not otherwise influence wave features. Application of the amplitude scaling relation to several historical events yields "predicted" near-field wave amplitudes in reasonable agreement with measurements and observations. Together, the scaling relations for near-field amplitude, wavelength, and submerged travel time provide key inputs necessary for computational wave propagation and hazards assessment. *INDEX TERMS:* 1845 Hydrology: Limnology; 1857 Hydrology: Reservoirs (surface); 4564 Oceanography: Physical: Tsunamis and storm surges; *KEYWORDS:* tsunamis, impulse waves, landslides, debris flows

Citation: Walder, J. S., P. Watts, O. E. Sorensen, and K. Janssen, Tsunamis generated by subaerial mass flows, *J. Geophys. Res.*, *108*(B5), 2236, doi:10.1029/2001JB000707, 2003.

1. Introduction

[2] Water waves can be generated by any sort of geophysical mass flow, including debris flows, debris avalanches, pyroclastic flows, landslides, and rockfalls, and pose significant hazards in a variety of settings. Tsunamis generated by submarine mass flows constitute a widely recognized hazardous phenomenon; some recent examples have been described by *Imamura and Gica* [1996], *Raichlen et al.* [1996], and *Tappin et al.* [1999, 2001]. However, destructive water waves are not restricted to the oceans: there are many pertinent examples from alpine environments [e.g., *Jørstad*, 1968; *Plafker and Eyzaguirre*, 1979; *Huber*, 1982; *Evans*, 1989]. A key motivation for the work reported here is improving our ability to assess water wave hazards in lakes and reservoirs likely to be affected by volcanogenic mass flows. The flanks of volcanoes are commonly host to large quantities of unconsolidated sediment and are especially prone to spawning mass flows, sometimes generated in the course of eruptive activity, but often during periods of volcanic quiescence as well [e.g., *Scott*, 2000]. In this paper we restrict our attention to water waves generated by mass flows that originate subaerially and do not interact thermally with water. We therefore specifically exclude the case of water wave generation by pyroclastic density currents, which commonly split into two components upon hitting a water body: one part plunges into the water while the other moves over the water surface [e.g., *Cas and Wright*, 1987; *Freundt*, 2001].

[3] For the sake of brevity, we will adopt several terminological simplifications. The term "tsunami" will be used

[1]Now at Department of Geological Engineering and Sciences, Michigan Technological University, Houghton, Michigan, USA.

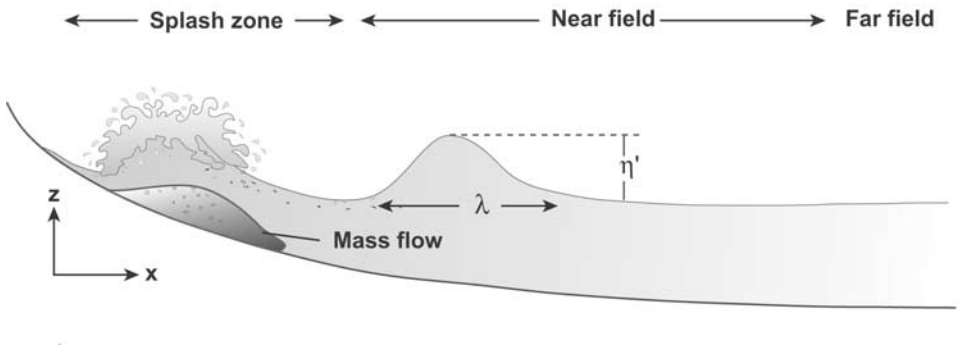

Figure 1. Sketch illustrating separation of splash zone, near field, and far field and definition of coordinates for scaling analysis. The water surface in the splash zone, the length of which is comparable to the landslide runout distance, is highly irregular. In the near field, water displaced by the landslide has organized itself into a coherent waveform, with the leading wave commonly being a broad hump of width [x] and amplitude η' relative to the ambient water surface. In the far field, dispersive effects become important.

to refer to impulsively generated water waves in surface water bodies as well as in the ocean, and the term ''landslide'' will be used to refer to all types of geophysical mass flows insofar as impulse wave generation is concerned. We emphasize that no genetic connotations should be attached to the latter word choice. Indeed, as we will argue below, near-field wave characteristics are, to leading order, independent of the type of mass flow involved. We also adopt the nomenclature of the tsunami and coastal engineering literature [e.g., *Dean and Dalrymple*, 1991] by using the term ''wave maker'' to refer to mass flows when our focus is on their role in generating water waves.

[4] In the context of customary tsunami modeling, to compute wave effects at any location, one would have to begin by calculating in detail the complicated fluid and solid motions caused by the wave maker plunging into water. Some attempts along these lines have been made [e.g., *Norem et al.*, 1990; *Imamura and Imteaz*, 1995; *Assier Rzadkiewicz et al.*, 1997], although it is unclear whether the interaction of the solid and fluid phases has been properly described [cf. *Iverson*, 1997; *Iverson and Denlinger*, 2001; *Iverson and Vallance*, 2001]. We take a different approach. We do not concern ourselves with the details of the wave maker's interaction with the water at impact; instead, we conceive of this zone of complicated solid/fluid interaction as a sort of ''black box'' out of which emerges a water wave with definable characteristics. This wave first exists in the near field (Figure 1), that is, in the region just beyond the point where the mass flow stops, but before propagation effects (dispersion, bathymetric refraction, and wave front spreading) come into play. (Issues associated with far-field wave propagation have been addressed by, e.g., *Ben-Menahem and Rosenman* [1972] and *Iwasaki* [1997].) Near-field wave characteristics, of course, implicitly derive from what goes on within the black box, and indeed we will show in section 2 just what ''outputs'' we require from the black box. Although the near-field region is spatially limited, it turns out that for many tsunamis in lakes, much of the domain of interest lies within the near field. Moreover, the fact that the tsunami has well-defined characteristics within this region means that the near field serves as a proxy ''source'' for computational wave propagation purposes. Thus we reach a powerful methodological conclusion: the wave propagation part of the tsunami problem can be carried out independently of the complicated exercise of computing splash zone dynamics, as long as one is willing to forego details of the state of affairs within the splash zone proper.

[5] The rest of this paper is organized as follows. In section 2, we demonstrate using scaling analysis that near-field wave characteristics should depend primarily on three parameters characterizing the wave maker: V_w^*, a dimensionless measure of volume; $\hat{\mathrm{Fr}}$, a dimensionless measure of maximum speed; t_s^*, a dimensionless measure of submerged travel time. The last of these is a proxy measure of splash zone dynamics. The role of wave maker time of motion has not previously been considered with regards to wave makers of subaerial origin, although it has factored into analyses of tsunami generation by earthquakes [*Hammack*, 1973] and submarine mass flows [*Watts*, 1997, 1998]. Sections 3 and 4 describe our experiments and data analysis methods, respectively. In section 5 we apply results of the scaling analysis to organize experimental data, not only ours but also, to the extent possible, some of the copious data presented in the theses of *Bowering* [1970] and *Huber* [1980]. We show that near-field wave amplitude may be variously described in terms of the dimensionless quantities identified by the scaling analyses but that not all these descriptions have equal merit. The most useful description gives dimensionless wave amplitude as a simple function of t_s^*/V_w^*, for diverse wave maker types and initial conditions. We also show that the characteristic wavelength of the experimental impulse waves follows the functional form indicated by the scaling analysis. In section 6 we show that the wave maker time of motion (a parameter that we measured, but which would have to be assigned in applying our results for prognostic purposes) can be related with reasonable accuracy to wave maker geometry. In section 7 we show that the experimentally based scaling relations yield ''predictions'' for several historical events that are in reasonable agreement with data.

2. Scaling Analysis of the Water Wave Equations

[6] Here we recast the governing partial differential equations for water wave propagation (the so-called Euler

equations) into dimensionless form to identify the quantities that control near-field wave amplitude. This formal exercise is needed because related theoretical studies [*Noda*, 1970; *Hunt*,1988; *Gozali and Hunt*, 1989; *Sander and Hutter*, 1992, 1996; *Villeneuve and Savage*, 1993] have not focused on near-field wave characteristics. The scaling analysis here is slightly didactic but for the problem at hand superior to simple dimensional analysis [e.g., *Law and Brebner*, 1968; *Kamphuis and Bowering*, 1970; *Huber*, 1980], which is apt to identify a plethora of parameters that play at best an indirect role and do not necessarily elucidate meaningful structure in experimental data. The scaling analysis provides novel information regarding water wave generation by mass flows even though we do not explicitly solve the Euler equations. The experimental results described later serve as an analog solution of the Euler equations and confirm predictions of the scaling analysis.

[7] We consider the two-dimensional geometry shown in Figure 1. The splash zone, or wave generation zone, is the region where landslide and water motion are coupled, and extends as far as the landslide travels. *Watts and Walder* [2003] have briefly discussed some theoretical aspects of splash zone hydrodynamics, and *Fritz et al.* [2001] have investigated the splash zone experimentally. We do not delve further into splash zone dynamics because our focus is not on splashing itself, but rather on the waveform that emerges from the splash zone. The near field may be defined as the region beyond the splash zone yet before the kinetic and potential energy of the wave train approach asymptotic values. For small-amplitude, linear waves, wave energy in the far field is equally partitioned between kinetic and potential energy [e.g., *Dean and Dalrymple*, 1991]. *Watts* [2000] found constant potential energy flux was first achieved, and the far field began, at a distance of about three wavelengths from the wave generation zone for linear water waves generated by subaqueous block landslides. For the large-amplitude, nonlinear waves of interest here, equipartition does not occur, but the far field will still be characterized by a steady partition between kinetic and potential energy. In applications of our results, we will suppose that an appropriate criterion is to classify the far field as beginning at a distance of about 3[x] beyond the impact zone, where [x] is the characteristic "width" of the waveform in the near field.

[8] Wave propagation is governed by the two-dimensional Euler equations for mass and momentum conservation in an incompressible liquid:

$$\frac{\partial u'}{\partial x'} + \frac{\partial w'}{\partial z'} = 0 \tag{1}$$

$$\frac{\partial u'}{\partial t'} + u'\frac{\partial u'}{\partial x'} + w'\frac{\partial u'}{\partial z'} = -\left(\frac{1}{\rho_w}\right)\frac{\partial p'}{\partial x'} \tag{2}$$

$$\frac{\partial w'}{\partial t'} + u'\frac{\partial w'}{\partial x'} + w'\frac{\partial w'}{\partial z'} = -\left(\frac{1}{\rho_w}\right)\frac{\partial p'}{\partial z'} - g \tag{3}$$

These equations are essentially the Navier-Stokes equations with viscosity neglected. This approximation is well established in analyses of wave generation and propagation [e.g., *Dean and Dalrymple*, 1991]. Viscous effects are important only within boundary layers and have negligible effect on wave maker motion at the large Reynolds numbers encountered in both the laboratory and in nature (Appendix C). Viscosity affects wave propagation again via boundary layer effects, which may be parameterized by way of a drag coefficient, but we need not be concerned with that here. The bottom of the channel ($z' = 0$) is impermeable, and the kinematic free surface boundary condition is

$$w' = \frac{\partial \eta'}{\partial t'} + u'\frac{\partial \eta'}{\partial x'} \qquad z' = \eta'(x', t') \tag{4}$$

Here u' and w' are the components of fluid motion in the x' and z' directions, respectively (Figure 1), t' is time, η' is wave amplitude, p' is water pressure, ρ_w is the density of water, and g is acceleration due to gravity. The equations have not been vertically averaged, as is sometimes appropriate for studying wave propagation in the far field. Generally, equation (4) would be complemented by dynamic free surface boundary conditions of stress continuity. In line with the inviscid assumption inherent in the Euler equations, the free surface cannot support shear stresses. The effect of surface tension on the normal stress balance at the free surface is negligible for wavelengths greater than about 20 mm (Appendix C).

[9] Equations (1)–(4) can be recast into dimensionless form by choosing characteristic values for both dependent and independent variables. We denote characteristic values by square brackets; dimensionless variables will be written the same as dimensional variables but with the prime dropped: for example, $x' = [x]x$. Our choice of scalings is inspired by both *Hammack*'s [1973] analysis of near-field waves generated by a vertical piston and *Watts'* [1997, 1998] analysis for near-field water waves generated by submarine landslides. The x and z directions must scale differently to capture the physics properly: the x direction scales with water wave features, while the z direction scales with landslide features. This differs from a scaling analysis done to elucidate far-field wave propagation [e.g., *Sander and Hutter*, 1992; *Villeneuve and Savage*, 1993]. The choice of scales depends upon the location of the landslide source and its behavior as it submerges. We will consider in detail two particular scenarios (Figure 2). In the first, the landslide hits the water with some initial velocity; the slope of the shore is presumed to be relatively gentle and so the landslide decelerates to rest. Physically, this corresponds to, say, a mass moving down a river valley and entering a lake or the ocean. In the second scenario, we consider a landslide with its toe at the shoreline and initially at rest. The mass then accelerates downward along a steep shore until it reaches an essentially flat bed. Physically, this corresponds to, say, a landslide entering a lake from a steep alpine slope. These two distinct cases, which correspond to the two sets of experiments discussed below, will be referred to as the initial velocity case and the release-from-shore case. One could obviously posit a sort of transitional case as well: a landslide released from a steep slope that accelerates subaerially, and continues to accelerate subaqueously, before coming to rest. We have not investigated the transitional

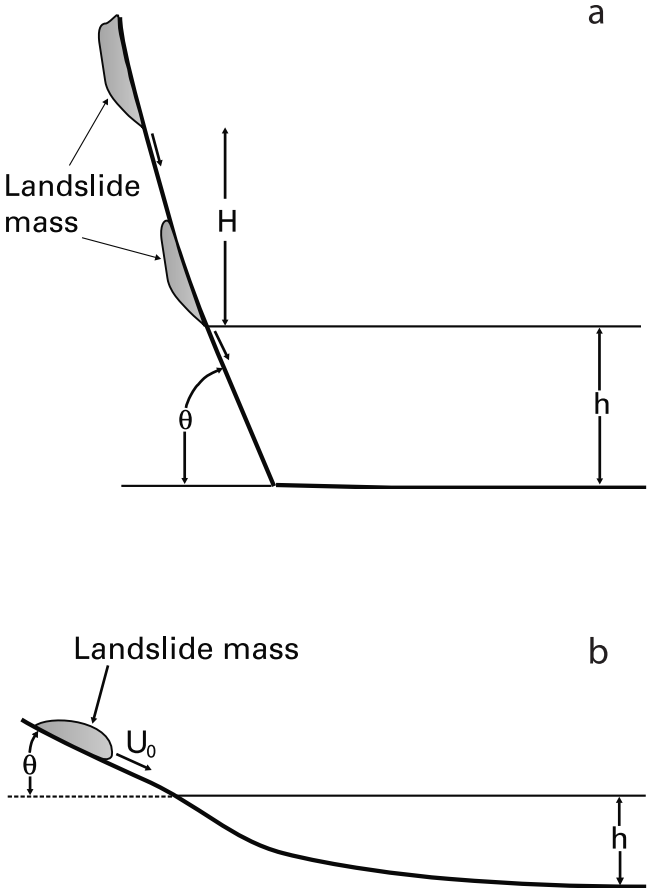

Figure 2. Landslide submergence scenarios considered in the scaling analyses. (a) A landslide mass enters a water body at initial speed U_0 and decelerates to rest in water of depth h. (b) A landslide mass released either at the shore or at a height H above water level accelerates down a steep slope and only decelerates when it reaches the bottom.

case experimentally, but we do present a simple analysis to show how it relates to the other two cases.

2.1. Initial Velocity Case

[10] Dimensionless variables for this case as appropriately defined as follows:

$$x' = [x]x = t_s\sqrt{gh}x$$

$$z' = hz$$

$$t' = [t]t$$

$$u' = \sqrt{gh}u$$

$$w' = (U_0 \sin\theta)w$$

$$p' = \rho_w gh\left(-z + \frac{[\eta]}{h}\eta(x)\right) + (\rho_w U_0^2 \sin^2\theta)p$$

$$\eta' = [\eta]\eta$$

where θ is the slope at the shoreline. The length scale $[x]$ may be interpreted as the distance over which water is displaced by long waves during the time of landslide motion and is thus a sort of wavelength. Speed in the x direction scales with the celerity of long waves, as that is the speed at which the wave front spreads [*Whitham*, 1974], while speed in the z direction scales with the vertical component of wave maker velocity at impact, U_0 being the block speed along its path at the time of entry into the water. The time scale $[t]$ is best chosen as the smaller of either t_w, the characteristic time for long waves to cross the wave propagation zone, or t_s, the characteristic time of submerged wave maker motion. We show in Appendix A that t_s is commonly smaller than t_w, and therefore choose $[t] = t_s$. (If the wave maker motion can be described simply by a uniform deceleration of magnitude α, then $t_s = U_0/\alpha$.) Pressure has been broken into two terms, the first being the hydrostatic component, which vanishes on the free surface, the second being the nonhydrostatic component. The characteristic wave amplitude, $[\eta]$, is specified [cf. *Watts*, 1998] by equating the volume of the wave "hump" in the near field to the volume displaced by the block. This conservation condition may be expressed as $[\eta][x]/2 \approx V_w$, where V_w is the submerged block volume per unit width, so we choose

$$[\eta] = \frac{2V_w}{t_s\sqrt{gh}}$$

We have made no special assumptions about wave maker motion and in particular do not assume, as was done by *Noda* [1970], *Das and Wiegel* [1972], and *Gozali and Hunt* [1989], that wave maker thickness exceeds water depth, with the wave maker effectively acting as a moving wall. Substituting the scales defined above into equations (1)–(4) yields

$$\frac{\partial u}{\partial x} + t_s^* \mathrm{Fr}\sin\theta\frac{\partial w}{\partial z} = 0 \tag{5}$$

$$\frac{\partial u}{\partial t} + u\frac{\partial u}{\partial x} + t_s^* \mathrm{Fr}\sin\theta w\frac{\partial u}{\partial z} = -\frac{2V_w^*}{t_s^*}\frac{\partial \eta}{\partial x} - \mathrm{Fr}^2\sin^2\theta\frac{\partial p}{\partial x} \tag{6}$$

$$\frac{\partial w}{\partial t} + u\frac{\partial w}{\partial x} + t_s^* \mathrm{Fr}\sin\theta w\frac{\partial w}{\partial z} = -t_s^* \mathrm{Fr}\sin\theta\frac{\partial p}{\partial z} \tag{7}$$

$$w = \frac{2V_w^*/t_s^*}{t_s^* \mathrm{Fr}\sin\theta}\left(\frac{\partial \eta}{\partial t} + u\frac{\partial \eta}{\partial x}\right) \qquad z = \left(\frac{2V_w^*}{t_s}\right)\eta \tag{8}$$

The dimensionless quantities that appear are slope angle θ as well as Fr, $t_s^* = t_s\sqrt{g/h}$, and $V_w^* = V_w/h^2$, which are dimensionless measures of, respectively, block impact speed, submerged travel time, and wave maker volume per unit width. Clearly t_s^* is an output from the splash zone "black box" and is a proxy measure of wave maker dynamics within the splash zone. Note that Fr (the initial wave maker Froude number) appears only in the combination Fr sin θ, a dimensionless measure of the vertical component of wave maker impact speed. Thus we predict that the dimensionless wave amplitude in the near field will be given in the functional form

$$\frac{\eta'}{[\eta]} = \eta = f(V_w^*, t_s^*, \mathrm{Fr}\sin\theta) \tag{9}$$

We further note that nondimensional wave maker volume appears in the scaled Euler equations not alone but rather as the ratio V_w^*/t_s^*. This ratio turns out to provide a very effective basis for collapsing experimental data.

2.2. Release-From-Shore Case

[11] In this case $U_0 = 0$ and the scaling of the initial velocity case cannot be applied. Instead we define dimensionless variables by

$$x' = [x]x = t_s\sqrt{gh}x$$

$$z' = hz$$

$$t' = [t]t$$

$$u' = \sqrt{gh}u$$

$$w' = (U_{\max}\sin\theta)w$$

$$p' = \rho_w gh\left(-z + \frac{[\eta]}{h}\eta(x)\right) + \left(\rho_w U_{\max}^2\sin^2\theta\right)p$$

$$[\eta] = \frac{2V_w}{t_s\sqrt{gh}}$$

where $U_{\max}$ is the maximum speed of the wave maker along the ramp of slope θ. (If the wave maker motion can be described simply by a uniform acceleration α, then $[t] \sim \sqrt{h/\alpha\sin\theta}$ and $U_{\max} \sim \sqrt{h\alpha/\sin\theta}$.) As with the initial velocity case, the timescale t_s characterizing wave maker motion is commonly smaller than t_w, the characteristic time for long waves to cross the wave propagation zone, and we therefore choose $[t] = t_s$ (see Appendix A). The dimensionless Euler equations therefore take the form

$$\frac{\partial u}{\partial x} + t_s^*\mathrm{Fr}_{\max}\sin\theta\frac{\partial w}{\partial z} = 0 \tag{10}$$

$$\frac{\partial u}{\partial t} + u\frac{\partial u}{\partial x} + t_s^*\mathrm{Fr}_{\max}\sin\theta w\frac{\partial u}{\partial z} = -\frac{2V_w^*}{t_s^*}\frac{\partial\eta}{\partial x} - \mathrm{Fr}_{\max}^2\sin^2\theta\frac{\partial p}{\partial x} \tag{11}$$

$$\frac{\partial w}{\partial t} + u\frac{\partial w}{\partial x} + t_s^*\mathrm{Fr}_{\max}\sin\theta w\frac{\partial w}{\partial z} = -t_s^*\mathrm{Fr}_{\max}\sin\theta\frac{\partial p}{\partial z} \tag{12}$$

$$w = \frac{2V_w^*/t_s}{t_s^*\mathrm{Fr}_{\max}\sin\theta}\left(\frac{\partial\eta}{\partial t} + u\frac{\partial\eta}{\partial x}\right) \quad z = \left(\frac{2V_w^*}{t_s}\right)\eta \tag{13}$$

with $\mathrm{Fr}_{\max}$ being the maximum value of wave maker Froude number achieved. We conclude that for the release-from-shore case,

$$\frac{\eta'}{[\eta]} = \eta = f(V_w^*, t_s^*, \mathrm{Fr}_{\max}\sin\theta) \tag{14}$$

Again we note that nondimensional wave maker volume appears in the scaled Euler equations not alone but rather as the ratio V_w^*/t_s^*.

2.3. Transitional Case

[12] A landslide released from a steep slope may of course originate up slope rather than exactly at the water's edge, and accelerate both subaerially and subaqueously before coming to rest. We do not present a formal scaling analysis of this scenario, but rather calculate in an approximate fashion how much the characteristic submerged travel time differs from the value found for the release-from-shore case. Consider a mass released at a height H above the shoreline (Figure 2) and assume that the mass accelerates down a slope of angle θ that extends below water level to a depth h. The characteristic acceleration is assumed to take the same value α both subaerially and subaqueously. (The implicit assumption here, anticipating a result to be presented later, is that motion is everywhere dominated by frictional forces.) The time τ_{ss} for a landslide released at the shoreline to reach the base is then $\sqrt{2h/\alpha\sin\theta}$, whereas the time τ_H for a landslide released at height H to reach the base is $\sqrt{2(h+H)/\alpha\sin\theta}$, with an amount $\sqrt{2H/\alpha\sin\theta}$ of that being subaerial. Letting τ_{sH} denote the submerged travel time of the landslide released at height H, we find

$$\frac{\tau_{sH}}{\tau_{ss}} = \left(\frac{H}{h} + 1\right)^{1/2} - \left(\frac{H}{h}\right)^{1/2} \tag{15}$$

This relation is illustrated graphically in Figure 3. The submerged travel time differs from τ_{ss} quite significantly for $H/h > ca.$ 1. Equivalently, one may say that the impact speed has a dominant effect on the submerged travel time, which is what enters the scaling analysis, for $H/h > ca.$ 1.

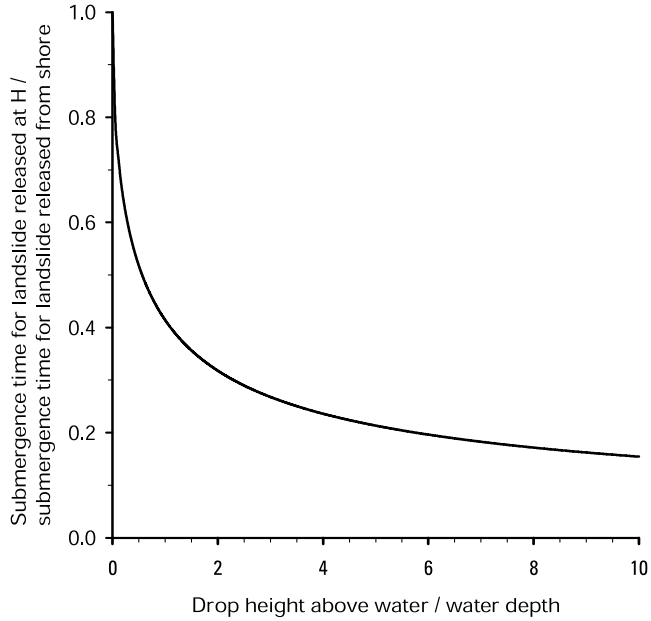

Figure 3. Ratio of τ_{sH} (submergence time for a landslide released at height H above water surface) to τ_{ss} (submergence time for a landslide released at the shore) as a function of H/h, where h is water depth. The effect of the speed acquired during subaerial movement dominates for H/h greater than $\sim$1.

2.4. Consequences of the Scaling Analysis

[13] Previous investigators [e.g., *Kamphuis and Bowering*, 1970; *Huber*, 1980] have tried, with limited success, to

represent dimensionless wave amplitude (both near-field and far-field) without reference to any measures of splash zone dynamics. For example, *Huber* [1980] correlated his data for both near field and far field in the form $\tilde{\eta} = CV_w^{*n}$, with C and n being functions of x. *Kamphuis and Bowering* [1970] considered dimensionless collapses of wave amplitude data in terms of V_w^* and Fr. We suggest on the basis of our scaling analysis that a proxy measure of splash zone dynamics, t_s^*, is likely to factor into a dimensionless collapse of experimental data via the ratio V_w^*/t_s^*. This ratio may be interpreted physically as a dimensionless measure of the landslide "flux" per unit width. It is also instructive to consider the *reciprocal* ratio t_s^*/V_w^*, which may be written as

$$\frac{t_s^*}{V_w^*} = \frac{t_s}{V_w/h\sqrt{gh}} \tag{16}$$

The speed of a parcel of water scales as $\sqrt{gh}$ [*Dean and Dalrymple*, 1991]; in the limiting case of bore formation, the volumetric rate of water transport per unit width is proportional to $h\sqrt{gh}$ [*Whitham*, 1974]. The time required for an impulse wave to displace a water volume equal to the wave maker volume therefore scales with $t_v = V_w/h\sqrt{gh}$. We expect that if t_s/t_v (or t_s^*/V_w^*) becomes small enough, the impulse wave must become bore-like and wave amplitude must become insensitive to details of landslide motion. Support for this conjecture comes from noting that $[\eta] = 2hV_w^*/t_s^*$ and rewriting wave amplitude as a fraction of water depth h:

$$\tilde{\eta} = \frac{\eta'}{h} = \frac{2}{t_s^*/V_w^*} f\left(V_w^*, t_s^*, \hat{\mathrm{Fr}}\sin\theta\right) \tag{17}$$

($\hat{\mathrm{Fr}}$ represents either Fr or $\mathrm{Fr}_{\max}$, whichever choice is pertinent.) It is known empirically that $\tilde{\eta}$ has a limiting value of about 0.85 for freely propagating solitary waves in a constant depth channel; for greater amplitudes, waves must eventually break [*Dean and Dalrymple*, 1991]. This physical upper bound on $\tilde{\eta}$ suggests that the function f must approach an asymptotic form for small enough values of t_s^*/V_w^*. Later we show by analysis of our data that this asymptote corresponds to $t_s^*/V_w^* \approx 2$.

[14] As the combination t_s^*/V_w^* involves both an input to the splash zone black box, namely, V_w^*, and an output from the black box, namely, t_s^*, it may at first seem to be a peculiar quantity to use for characterizing wave amplitude. However, the usefulness of an analogous quantity for characterizing wave amplitude has been previously shown by *Watts* [1997, 1998] for the case of underwater landslides. Moreover, t_s^* may be calculated from measurable quantities and, as we shall demonstrate, may be reasonably estimated in terms of a black-box input not yet considered: landslide geometry. We return to this important point later.

3. Experimental Methods

[15] Laboratory studies of landslide-generated water waves have been done before, notably by *Law and Brebner* [1968], *Bowering* [1970], *Das and Wiegel* [1972], *Kamphuis and Bowering* [1970], *Huber* [1980], and *Sander and Hutter* [1992, 1996]. However, none of these investigators focused on what controlled the characteristics of waves in the near field. Our experiments were done with an eye toward answering a simple question: Can near-field wave features such as amplitude and wavelength be predicted? If so, they can be used to specify a "tsunami source" for computational wave propagation simulations and hazards assessment.

[16] We did two sets of experiments with rigid wave makers. The initial velocity experiments involved solid blocks sliding down a flume into a body of water impounded at the base. The release-from-shore experiments involved either solid blocks or a solid cylinder released at the "shoreline" and allowed to move down a ramp into a constant depth tank. Experimental data and derived quantities are tabulated in an electronic supplement.

3.1. Initial Velocity Experiments

[17] The flume bed curved smoothly to become the bed of a constant depth tank (Figure 4): this geometry approximates what would be found in nature where a stream channel enters a lake. Owing to space limitations, the constant depth water tank was only slightly more than 1 m long, far too short to investigate, say, dispersive effects during wave propagation, but adequate for measuring near-field characteristics of the leading wave generated by a block. The tank width was 285 mm.

[18] Blocks were constructed by attaching a tapered solid piece of Nylon with a triangular cross section to a hollow box of rectangular cross section, also made of Nylon (Figure 5). All blocks had a front tapered at about 32°. We used blocks with a thickness T of either 31 mm or 51 mm, width W of 150 mm, and length L ranging from 94 to 401 mm. Block volumes were known to within about 3%. Each hollow box was filled with sand or lead pellets and weighed on an analytical balance accurate to 0.1 g to achieve a desired bulk specific gravity. All experiments reported here used blocks with a bulk specific gravity of 2.9. This is somewhat higher than expected for actual geophysical flows, but was used to assure that (as discussed in Appendix B) impulsive slowing of the blocks as they contacted the water would be negligible.

[19] Blocks were constrained as they moved down the flume by Nylon walls, which flared outward toward the Plexiglas tank walls where the blocks entered the water (Figure 4). This arrangement minimized block twisting and at the same time permitted the use of videography through the Plexiglas walls to measure wave amplitude. A wire mesh screen was attached to the tank walls 1 m from the downstream end of the constant depth tank (Figure 4). In some experiments with relatively shallow water and/or high impact speeds, the blocks reached the screen, but more commonly the blocks stopped short of the screen. Reflections from the downstream end of the tank were damped by using several thicknesses of woven fabric (household furnace filters).

[20] In some experiments with the shortest blocks at relatively high speeds, we observed anomalous behavior probably related to hydroplaning [cf. *Mohrig et al.*, 1998]: the snout of the fully submerged block would rapidly flip up from the bed of the flume, sometimes so vigorously as to make the block flip over entirely. This

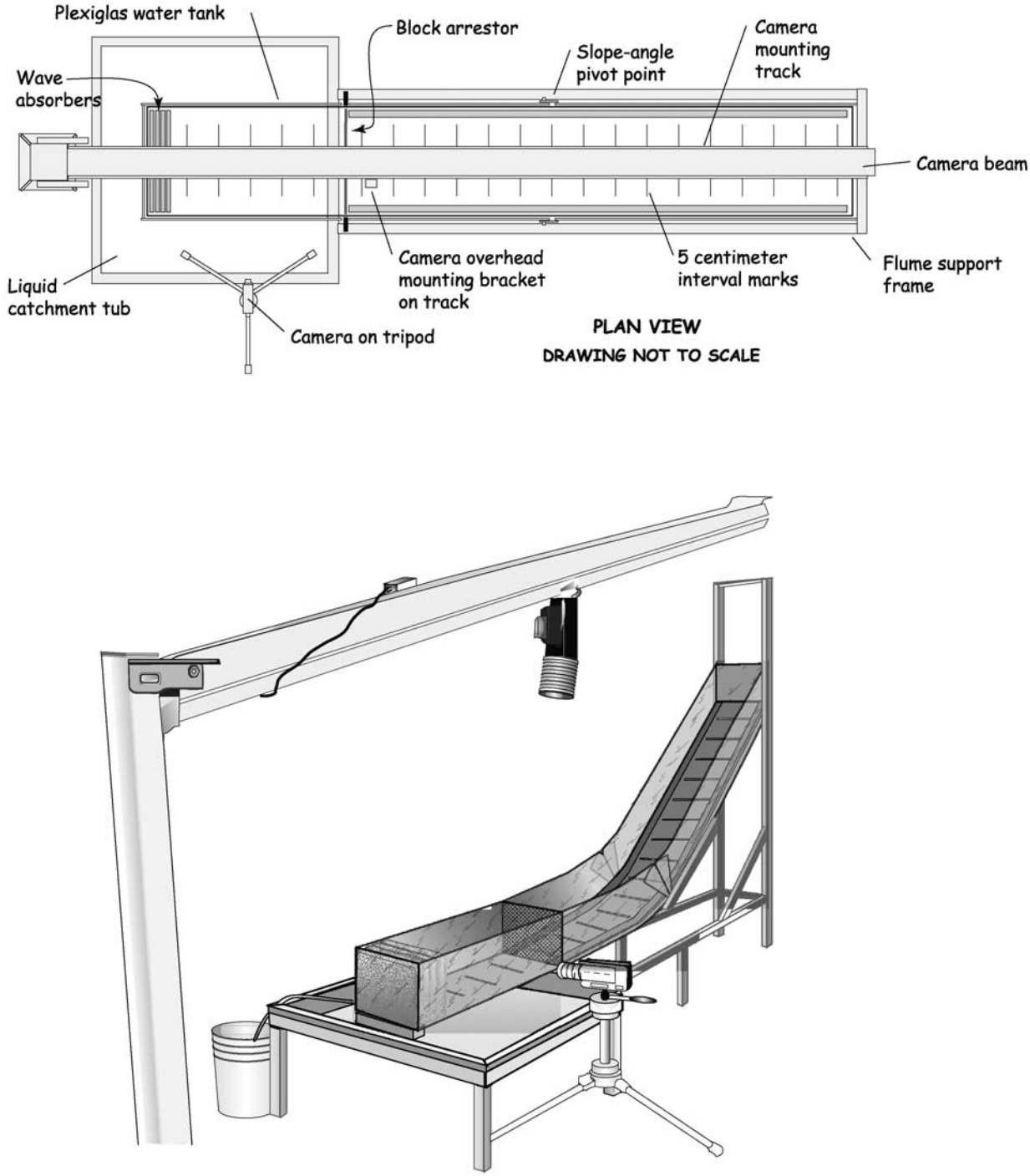

Figure 4. Experimental flume for the initial velocity tests. The oblique view of the flume shows how the constant slope track smoothly curved to join the horizontal bed of the constant depth tank.

behavior obviously had a strong effect on block motion and water wave formation, so we discarded results of these experiments.

[21] Experiments were done for three different water depths in the constant depth tank: 51 mm, 90 mm and 130 mm. Corresponding values of shoreline slope were 11.2°, 15°, and 19.5°. (Because of the simple flume construction, water depth and shoreline slope could not be independently varied in any convenient way.) Note that in all experiments the block thickness was a substantial fraction (0.24 to 1) of the water depth in the constant depth tank. In practice, this meant that the water surface in the wave generation zone (i.e., above the moving block) was fairly irregular and that a clearly defined leading wave "hump" only became apparent once the block had slowed considerably. Although we used fairly shallow water, we expect surface tension effects to have been negligible (Appendix C).

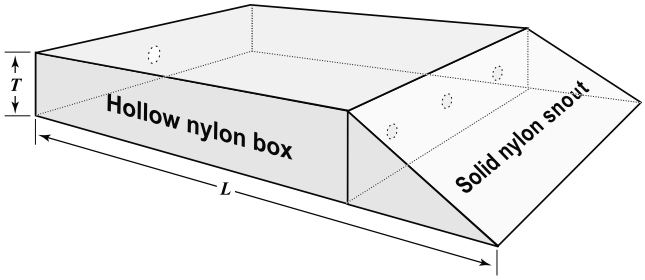

Figure 5. Geometry of the experimental blocks. The snout was tapered at an angle of 32°.

[22] The scaling analysis suggested that, all else being held constant, the vertical component of block impact velocity (expressed as Fr sin θ) might affect wave amplitude. Thus we needed to be able to prescribe Fr for any set of experiments with a fixed slope. To this end, we determined empirically for each block how impact speed depended on the point at which the block was released. Impact speeds were in typically in the range of about 1 to 3.5 m/s, corresponding to Fr $\approx$ 1–4, depending on water depth. For each block, impact speed was determined for at least 6 release points along the flume, and a quadratic polynomial was fitted to the data. In this way we would then pick a release point corresponding to a desired impact speed (or Fr). We estimate the error in the impact speed determined this way to be no more than 0.1 to 0.2 m/s, with the error greatest for the highest impact speeds.

[23] Block motion was recorded from above by a digital video camera, with reference lines along the flume bed at an interval of 50 mm. The camera's field of view was adjusted so as capture most of the submerged motion. The images were subsequently analyzed frame by frame to determine block position as a function of time. The amplitude of the leading wave was measured by placing another video camera 0.5 m from the downstream end of the constant depth tank (Figure 4). This corresponds to a distance of about 1.0 m, or 8 to 20 times the water depth, from the point at which the Nylon walls flared outward toward the Plexiglas flume walls. Wave front spreading associated with the flared region was accomplished before the wave reaches the camera's field of view. As we will later show, the camera for measuring wave amplitude was a distance $O([x])$ downstream of the wave generation zone, and a comparable distance from the end of the constant depth tank. We verified empirically that moving the video camera sideways by 0.1 m (corresponding to about 20–40% of $[x]$) in either direction did not affect the measured wave amplitude. Wave amplitude was measured with reference to a set of parallel lines spaced 5 mm apart on the inside (i.e., wetted) wall of the flume.

3.2. Release-From-Shore Experiments

[24] These experiments were done using a glass-walled rectangular tank 1 m high, 6 m long, and 200 mm wide. A Nylon ramp inclined at 30° from the horizontal was placed inside the tank near one end. The wave makers used in most experiments were the same Nylon blocks described above, although in a minority of experiments the wave maker was a solid steel cylinder 50 mm in diameter and 144 mm long. Block weights were varied by filling the hollow portion with varying amounts of sand or steel pellets. Various water depths were used. (Details may be found in the auxiliary material[1].) The wave makers were held against the ramp such that they were just barely touching the water surface, then released. Raised edges on the ramp kept the wave maker from twisting. The blocks invariably slammed into the base of the tank and came to a nearly complete stop, with subsequent motion consisting of a slow slumping toward the horizontal. The cylinder, in contrast, would continue beyond the bottom of the ramp and roll some distance along the base of the tank. Wave maker motion along the ramp was videotaped through the sidewall of the tank, with a square grid of lines at 5 mm spacing for reference. A second video camera was placed at a distance $O([x])$ beyond the end of the wave generation zone, and wave amplitude was measured with reference to a set of parallel lines spaced 5 mm apart on the inside (i.e., wetted) wall of the tank.

4. Data Analysis

[25] Digital video images of every experimental run were transferred to a computer using an IEEE 1394 format interface card and then inspected to characterize wave maker motion and measure the amplitude of the leading wave. We also measured wave profile (i.e., surface elevation vs. distance) for a subset of experiments in order to characterize wavelength.

4.1. Wave Maker Motion

[26] Video images for any given experimental run were inspected frame by frame, and a number of individual frames were then "captured" and printed to measure wave maker front position as a function of time. (Framing rate was 30 per second.) Error in wave maker position derives from both image resolution (one pixel corresponds to about 1.5 mm) and image blur (from the finite exposure time). For the initial velocity experiments, we estimate the probable error in measured wave maker position to be about 3 to 4 mm at relatively low impact speeds but as much as 10 to 15 mm at the highest impact speeds. For the release-from-shore experiments, the wave maker speeds achieved are never very great and we estimate the probable error in wave maker position to be about 3 to 4 mm.

[27] Determining the submerged travel time t_s by direct inspection of the videotapes turned out to be particularly problematic for the initial velocity tests because neither the precise moment of impact nor the precise time at which block motion stops can be picked. Impact time has to be interpolated, a procedure that is especially prone to error when the impact speed is relatively high. Picking the time at which motion stops involves equally challenging interpolation. We opted instead to determine t_s indirectly for the initial velocity tests. The position of the front of the wave

[1] Auxiliary data tables and figures are available via Web browser or via Anonymous FTP from ftp://ftp.agu.org, directory "append" (Username = "anonymous", Password = "guest"); subdirectories in the ftp site are arranged by paper number. Information on searching and submitting electronic supplements is found at http://www.agu.org/pubs/esupp_about.html.

maker as a function of time may always be written, for small enough times after impact, by the leading terms in a Taylor series expansion:

$$s'(t') = \upsilon t' + \left(\frac{1}{2}\right)\alpha t'^2 \tag{18}$$

where $s'(0) = 0$ by definition and α is a characteristic measure of block acceleration along the flow path (negative for the initial velocity experiments, positive for the release-from-shore experiments). Equation (18) provides a good fit to measured block displacement data in the initial velocity tests, so the characteristic time of motion for these experiments was taken as $t_s = \upsilon/|\alpha|$. Values so obtained compare quite well with t_s values estimated by direct examination of a sample of videotape records.

[28] For the release-from-shore experiments, U_0 is of course zero and we faced the task of determining t_s (reasonably taken as the time for the wave maker to reach the bottom of the ramp) and $U_{\max}$. If the wave maker underwent a constant acceleration-representing physically, say, the case in which solid/solid friction at the base were the dominant force resisting motion-then we would find from equation (18) that $t_s = \sqrt{2h/\alpha \sin\theta}$, $U_{\max} = \sqrt{2h\alpha/\sin\theta}$. Alternatively, if hydrodynamic drag dominated, the wave maker would asymptotically approach a terminal velocity, with the motion described by $s'(t') = s_0 \ln[\cosh(t'/t_0)]$ and the maximum (terminal) velocity given by $U_{\max} = s_0/t_0$, where s_0 and t_0 are fitting coefficients found by regression [*Watts*, 1997, 1998]. Each idealized case represents some data fairly well, but no single simple function $s'(t')$ adequately represents all the release-from-shore data. Accordingly, we chose to estimate t_s directly from the videotapes, but to estimate $U_{\max}$ from the derivative of ideal curves fitted to displacement data. (The alternative of calculating $U_{\max}$ from displacement data using finite differences would have been exceptionally time consuming and also poorly constrained, owing to the relatively large errors in locating block front as a function of time.)

4.2. Wave Amplitude

[29] Video images were inspected frame-by-frame and 1 or 2 then "captured" and printed to measure the amplitude of the leading wave, which was usually a broad, gentle, and reasonably symmetrical "swell", although in some experiments with very shallow water and relatively high impact speeds, leading waves had fairly steep leading faces and sometimes even showed incipient signs of breaking. The wave amplitude reported here is the maximum water surface elevation relative to the datum (still water). Error in measured wave amplitude derives from image resolution (0.4 mm per pixel) and image blur (from the finite exposure time). We estimate the probable error as being typically in the range 1 to 2 mm.

4.3. Profile of the Leading Wave

[30] For 12 experiments of each type, we measured surface height as a function of position on the leading wave, with measurements at typically 12 to 20 points used to define a characteristic "wavelength". This "wavelength" must be understood as a characteristic measure of the width of the leading wave hump, not as a peak-to-peak distance, as for sinusoidal waves. Because the leading wave was, in the great majority of cases, close to a symmetrical hump, we defined "wavelength" λ by using a fitting function $A\,\mathrm{sech}^2(x/\lambda)$, with A and λ being simply fitting coefficients determined by least squares regression. We emphasize that our choice of fitting function must not be construed as implying that the waveforms were solitary waves; for true solitary waves, which are finite amplitude waveforms that travel without change in shape, λ has a specific functional dependence on wave amplitude and water depth [e.g., *Dean and Dalrymple*, 1991, p. 315].

5. Measured Wave Characteristics and Data Collapse in Dimensionless Parameter Space

[31] The near-field wave must be characterized in terms of both amplitude and "wavelength" to provide necessary information for computational wave propagation. (A complete tsunami source description also requires knowledge of water velocity beneath the wave so that kinetic energy is properly accounted for.) Key results are summarized next; complete details regarding measured and derived quantities are tabulated in the auxiliary material.

5.1. Wave Amplitude

[32] We begin by considering whether it is actually possible [cf. *Kamphuis and Bowering*, 1970; *Huber*, 1980] to characterize dimensionless near-field wave amplitude without accounting for some measure of wave maker dynamics-in other words, whether it is possible to achieve a data collapse in the form

$$\tilde{\eta} = f\left(V_w^*, \hat{\mathrm{Fr}}\sin\theta\right) \tag{19}$$

and more particularly as

$$\tilde{\eta} = A V_w^{*m} (\mathrm{Fr}\sin\theta)^n \tag{20}$$

We used multiple linear regression applied to log-transformed quantities to find best fit values of the coefficient A and the exponents n and m. Results are shown in Table 1 for our data as well as data of *Bowering* [1970] and *Huber* [1980]. The key thing to note is that the fitting parameters take distinctly different values for each data set: there is no universal function of the form of equation (20) that holds for diverse wave makers and initial conditions. This is perhaps not surprising, as each set of experiments involved different wave maker materials and geometries. As there is no obvious way to decide which set of parameter values (if any) in Table 1 would apply to actual geophysical mass flows, we suggest that a relationship such as equation (20) is not useful for prognostic purposes with diverse wave makers.

[33] The next question to pose is whether a "universal" data collapse can be obtained if we factor in some measure of wave maker dynamics. The simplest functional form we might plausibly consider (as it brings in wave maker volume as well) is

$$\tilde{\eta} = f(t_s^*/V_w^*) \tag{21}$$

Table 1. Regression Coefficients[a]

	A	m	n	B	q	r
Our experiments	0.36	0.40	0.50	0.20	0.51	0.26
Bowering	1.06	1.33	0.92	1.53	1.33	−0.92
Huber	0.46	0.31	0.25	0.76	0.35	−0.32

[a]Coefficients refer to the fitting relations for nondimensional wave amplitude in equations (20) and (23), namely, $\tilde{\eta} = AV_w^{*m}(\mathrm{Fr}\sin\theta)^n$ and $\tilde{\eta} = BV_w^{*q}t_s^{*r}$. The wide disparity in exponent values makes it clear that neither of these regression relations is useful in a "universal" sense for collapsing wave maker data for diverse wave maker types and initial conditions. Equation (22), in contrast, does provide a reasonable "universal" fit to data.

In Figure 6 we show a plot of $\tilde{\eta}$ as a function of t_s^*/V_w^* for our experiments as well as a subset of those of *Bowering* [1970] and *Huber* [1980]. (Neither Bowering and Huber actually measured t_s, but we inferred t_s values from their tabulated data; our methods for doing so are described in Appendix D.) The experimental data have not been sorted in terms of $\hat{\mathrm{Fr}}$ sin θ (which ranged from about 0.35 to 1.75 for our experiments, and to even larger values for Bowering's and Huber's experiments). Data from all the experiments appear to follow the same trend within the intrinsic scatter. This result is somewhat remarkable when one considers that the various sets of experiments involved two distinct initial conditions (initial velocity or release from shore) and wave makers that varied greatly in terms of material type, geometry, rigidity, and specific gravity. Nonetheless, to first order, dimensionless wave amplitude $\tilde{\eta}$ in the near field

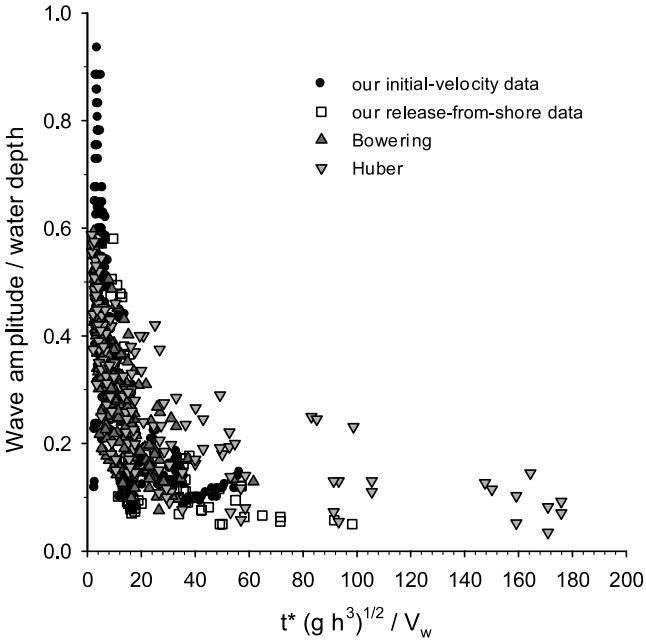

Figure 6. Plot of dimensionless wave amplitude as a function of t_s^*/V_w^* for our experiments and those of *Bowering* [1970] and *Huber* [1980]. Method of estimating t_s^* values for Bowering's and Huber's experiments is described in Appendix C. To avoid clutter, we do not show error bars, but note that the following error estimates apply: t_s^*/V_w^* is known to within ∼30% for our experiments and to within ∼40% for Bowering's and Huber's experiments; dimensionless wave amplitude is known to within ∼10% for all the data. See color version of this figure in the HTML.

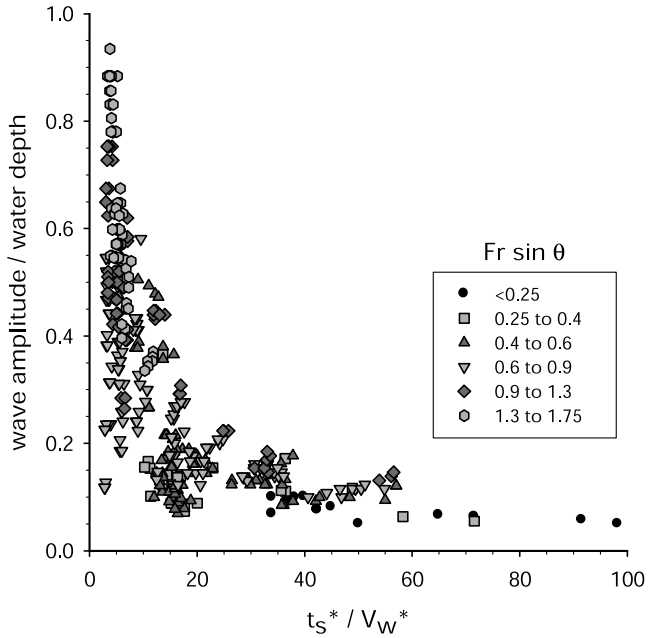

Figure 7. Plots of dimensionless wave amplitude as a function of t_s^*/V_w^*, with the data sorted in terms of Fr sin θ, for our experiments only. There is little clear dependence of dimensionless wave amplitude on Fr sin θ. See color version of this figure in the HTML.

for these diverse wave makers may be expressed as a simple function of t_s^*/V_w^*:

$$\tilde{\eta} = A(t_s^*/V_w^*)^{-b} \tag{22}$$

where A and b are empirically determined coefficients. A least squares fit to the log-transformed data yields $A = 1.32$, $b = 0.68$, with correlation coefficient $r^2 = 0.66$. (The regression is based on our data alone owing to the inferential nature of the t_s values for Huber's and Bowering's experiments.) Equation (22) is only valid up to the asymptotic (breaking wave) value $\tilde{\eta} \approx 0.85$, which corresponds to $t_s^*/V_w^* \approx 2$.

[34] An obvious alternative to equation (22) that also accounts for wave maker dynamics, in principle, is

$$\tilde{\eta} = Bt_s^{*q}V_w^{*r} \tag{23}$$

with the exponents determined by regression. Best fit coefficients for the several data sets are given in Table 1. The (q, r) values are widely divergent from one data set to another and this sort of procedure clearly does not lead to a universal data collapse.

[35] Although it seems fairly clear from Figure 6 that the quantity t_s^*/V_w^* does provide a physically meaningful basis for collapsing experimental data, we have also explored possible second-order dependence on Fr sin θ. In Figure 7 we again show our data for $\tilde{\eta}$ as a function of t_s^*/V_w^* but with the data sorted into finite-sized "bins" for Fr sin θ. There is no clear evidence of a second-order dependence of $\tilde{\eta}$ on Fr sin θ.

5.2. Wavelength

[36] In the near field, distances in the x direction scale with $t_s\sqrt{gh}$, so our measure of "wavelength" should scale

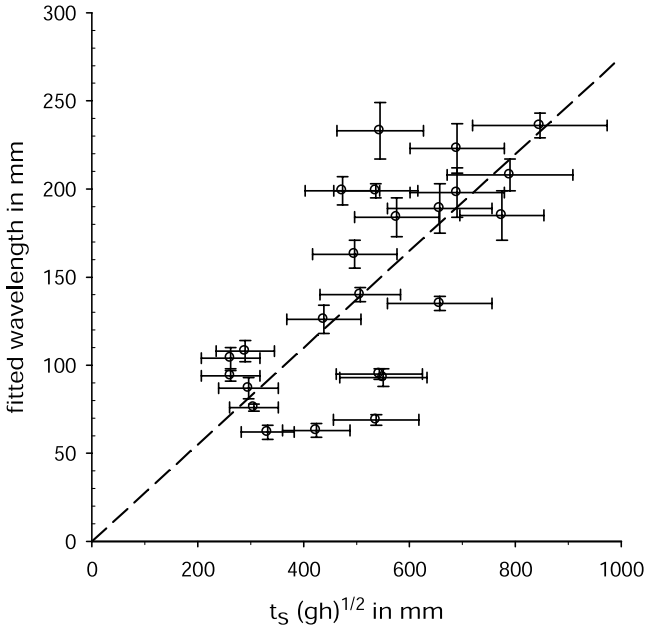

Figure 8. The fitted "wavelength" λ for a subset of our experiments as a function of the characteristic length scale in the direction of wave propagation. The fitted regression line follows from the scaling analysis. See color version of this figure in the HTML.

likewise. In Figure 8 we show "wavelength" λ, as defined by the curve-fitting scheme described above, as a function of $t_s\sqrt{gh}$. Given the error bars on the data points, the trends for the two sets of experiments cannot be distinguished. A least squares fit to the entire data set gives the result

$$\lambda = 0.27 t_s \sqrt{gh} = 0.27[x] \tag{24}$$

or equivalently in dimensionless form,

$$\frac{\lambda}{h} = 0.27 t_s^* = 0.27 \frac{[x]}{h} \tag{25}$$

Equations (22) and (25) together suffice to specify the tsunami shape in the near field. Note that assuming a wave shape different from $\mathrm{sech}^2(x/\lambda)$, as long as it is still symmetrical about the wave crest, would simply change the numerical constant in equation (24).

[37] Wavelengths reported by *Bowering* [1972] and *Huber* [1980] are not directly compared with our own measurements. Both those investigators defined wavelength in terms of characteristics of the entire wave train. *Bowering* [1972] presented some summary plots of wavelength defined as "twice the approximate distance from the first to the second zero crossing". Bowering's wavelength so defined had a value typically about $10h$ to $15h$, but it is unclear where this was measured along the channel. *Huber* [1980] defined wavelength as the distance from half the leading-wave amplitude to the second zero crossing, and the data for his gauge nearest the splash zone indicate wavelength typically about $4h$ to $8h$.

5.3. Other Water Wave Features

[38] We did not set out to measure the complete tsunami waveform or to investigate waveform evolution during wave propagation. Nonetheless, we can make some useful generalizations about the near-field waveform that would be important for computational wave propagation purposes. We note from our tabulated data (see the electronic supplement) that $[x]/h$ was in the range of about 4 to 12 (mean 6.8, standard deviation 2.4). This $[x]/h$ value corresponds to wavelengths intermediate between those of deep-water waves that never "feel" the bed and shallow-water waves with a celerity $\sqrt{gh}$ independent of wavelength. Clearly these impulse waves are dispersive. They are also moderately to strongly nonlinear, as indicated by the relatively large values (around 1 to 100) of the Ursell parameter $\mathrm{Ur} = (\eta'/h)([x]/h)^2$, which is commonly interpreted as the ratio of nonlinear effects to dispersive effects [e.g., *Lighthill*, 1978, pp. 463–464]. Any computational wave propagation scheme must therefore be able to account adequately for the effects of both dispersion and nonlinearity.

6. Submerged Time of Motion: Inferences About Splash Zone Dynamics

[39] Our black-box treatment of the splash zone has been very productive but has one troublesome aspect as we consider possible application of the results for prognostic purposes: geological reasoning, along with bathymetry, can provide reasonable estimates for probable values of V_w^* (we will say more about this in section 7), but we also must prescribe the nondimensional time of motion, t_s^*. Experimentally this parameter varied over a factor of about 5, and it is not at all obvious how to assign a value of t_s^* for predicting the characteristics of a wave produced by a hypothetical landslide. Surprisingly, we can make some progress in this direction by examining the experimentally determined values of t_s^* in the context of an idealized equation describing block-landslide motion in the splash zone. The approach is similar to that used by *Watts* [1997, 1998] in his study of subaqueous landslides but generalized to account in an approximate way for partial submergence of the solid mass as it enters the water. Thus we take s' as the position of the front of the block, reckoned positive from the shoreline toward deeper water, and t' as elapsed time from the moment the leading edge of the block enters the water. The driving force for landslide motion is simply gravity; motion is resisted by friction between the landslide and its bed, by hydrodynamic drag, and by the added mass effect. An approximate equation of motion is

$$\left(\gamma + \frac{C_m s'}{L}\right)\frac{d^2 s'}{dt'^2} = (\gamma - 1) g \chi \left(\frac{s'}{L}\right) + \gamma \chi g \left(1 - \frac{s'}{L}\right) - \left(\frac{C_d}{2L}\right)\left(\frac{ds'}{dt'}\right)^2 \tag{26}$$

where γ is specific gravity of the landslide, C_m is the so-called added mass coefficient, C_d is a drag coefficient, L is landslide length, $\chi = \sin\theta(1 - \tan\phi/\tan\theta)$, and ϕ is the dynamic bed friction angle. The first term on the right-hand side of equation (26) represents the down-slope component of the gravitational and frictional forces acting on the submerged part of the landslide; the second term on the right-hand side represents the down-slope component of the gravitational and frictional forces acting on the subaerial part of the landslide; the last term on the right-hand side represents hydrodynamic drag. The various

coefficients may be considered constants as a first approximation. When the landslide becomes fully submerged for (approximately) $s' \geq L$, s'/L should be set equal to one wherever it appears in a coefficient.

[40] We recast equation (26) into dimensionless form by choosing scales different from those used to scale the water wave equations but appropriate for characterizing landslide motion for the initial velocity case:

$$[s] = \frac{2L(\gamma + C_m)}{C_d} \tag{27a}$$

$$[t]_2 = (\gamma + C_m)\sqrt{\frac{2L}{(\gamma - 1)gC_d}} \tag{27b}$$

The equation of motion in dimensionless form becomes, after some rearrangement,

$$\frac{[\gamma + 2(\gamma + C_m)(C_m/C_d)s]}{\gamma + C_m}\frac{d^2s}{dt^2} = \frac{\chi[\gamma - 2(\gamma + C_m)s/C_d]}{(\gamma - 1)} - \left(\frac{ds}{dt}\right)^2 \tag{28}$$

with the proviso that for full submergence s is set equal to 1 wherever it appears in a coefficient or algebraic term. Any dimensionless measure of landslide motion will in general depend on the dimensionless coefficients that appear in equation (28); in particular (recalling the definition of χ) $t_s/[t]_2 = f(\gamma, C_m, C_d, \phi, \theta)$ and thus

$$t_s^* = \left(\frac{L}{h}\right)^{1/2} f(\gamma, C_m, C_d, \phi, \theta) \tag{29}$$

The coefficients C_m and C_d may be expected to depend on geometrical quantities (L/h, T/h, θ and the angle of taper of the block front) and an appropriately defined landslide Reynolds number Re. In our experiments, $Re \sim 10^5$, so we expect rapid boundary layer formation and negligible skin friction (Appendix C); Re should have little influence on either C_m or C_d during most of the block motion [*Watts*, 1997, 1998]. Specific gravity γ was held constant in the initial velocity experiments. The dynamic friction angle ϕ should vary little since all blocks were made of the same material. and entry slope varied only modestly. Thus we might expect that for our experiments, at least as a first approximation,

$$t_s^* \approx C_s(\theta)\left(\frac{L}{h}\right)^{0.5} \tag{30}$$

for the initial velocity experiments, where C_s is empirically determined.

[41] Figure 9 shows time-of-motion data for our experiments. There is no clear evidence that C_s varies with θ, but any dependence on θ may have been masked because θ and h could not really be varied independently in our simple flume. (Over the range of depths used, θ varied from 11.2° to 19.5°.) A best fit to log-transformed data for all slope angles gives the result $t_s^* = 4.8(L/h)^{0.40}$, but a regression fit with the exponent forced to be 0.5 also describes the data quite well, with $C_s = 4.5$. It is noteworthy that the exponent

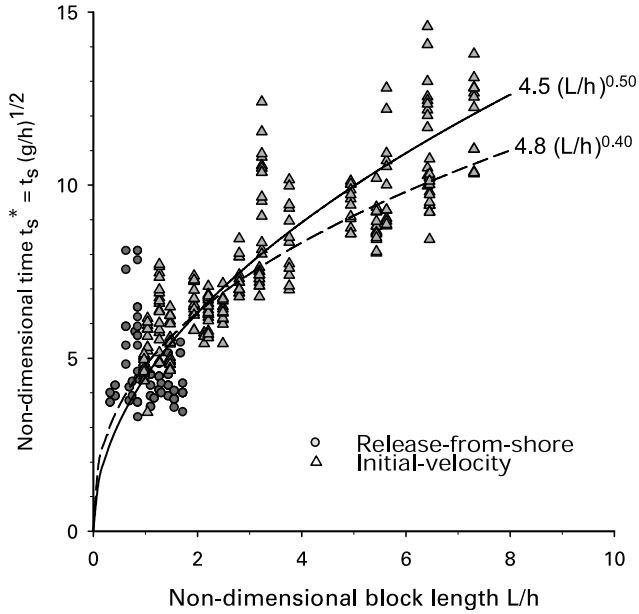

Figure 9. Dimensionless wave maker submergence time t_s^* for both the initial velocity experiments and the release-from-shore experiments, as a function of dimensionless wave maker length L/h. The curve shows a fit of the data to an assumed, simplified functional form $t_s^* = \text{const}\ (L/h)^{1/2}$, which would be expected if wave maker motion is controlled by frictional forces. See color version of this figure in the HTML.

0.5 would be expected in the case of a Coulomb frictional grain flow [*Savage and Hutter*, 1989]. It thus appears that submerged block-landslide motion is resisted primarily by frictional forces and only to a minor degree by hydrodynamic drag.

[42] Actual mass flows are not, of course, solid blocks as in our experiments. Nonetheless, we conclude that in general, the effects of specific gravity, wave maker geometry, and wave maker rheology on tsunami generation are all implicitly subsumed by t_s^*, which must be specified in some fashion. In principle, one should be able to predict t_s^* using a physically based model of mass flow interaction with water, along with pertinent bathymetric data. Diverse models of mass flow-generated tsunamis proposed to date [e.g., *Norem et al.*, 1990; *Heinrich*, 1991, 1992; *Jiang and LeBlond*, 1992, 1993, 1994; *Imamura and Imteaz*, 1995; *Assier Rzadkiewicz et al.*, 1997] all seemingly invoke rheological assumptions at odds with recent advances in our understanding of the actual mechanics of mass flows [*Iverson*, 1997; *Iverson and Vallance*, 2001]. We suggest that the most rigorous way to come up with true predictions of t_s^* would involve coupling the Euler equations to the mass flow model of *Iverson and Denlinger* [2001] and *Denlinger and Iverson* [2001], who treat mass flows as variably fluidized mixtures of solid grains and interstitial fluid. This would undoubtedly be a computationally challenging task.

[43] A scaling effect may arise for very large mass flows if the effective friction angle ϕ with flow volume [e.g., *Kilburn and Sørensen*, 1998]. Note that $[t]_2$, and thus t_s^*,

must increase as ϕecreases. From equation (27b), a decrease in ϕ from, say, 30° to 15° would increase t_s^* by a factor of about 1.5. An increase in t_s^* for a given landslide volume would have the effect of reducing water wave amplitude. However, the nature of long-runout landslides remains rather controversial, so "correcting" our scaling relationships would be at best a speculative exercise, and we demur.

7. Discussion

[44] Our goal in this work has been to examine experimental results in light of a rigorous scaling analysis. Our key result, imbedded in equations (22) and (25), is that the amplitude and shape of a tsunami in the near field may be fully specified, to an excellent approximation, in terms of three simple parameters: water depth, Wave maker volume, and the duration of submerged landslide motion. The last of these in turn may be expressed approximately in terms of wave maker length by equation (30).

[45] Experimental water wave measurements typically provide only first-order results owing to experimental errors that accumulate in dimensionless quantities. Such errors are minimized at great expense of time and effort. Our wave amplitude data do not obviously harbor a second-order trend (in nondimensional space), namely, dependence on Fr sin θ. The data of *Bowering* [1970] and *Huber* [1980] do appear to contain weak second-order dependence on Fr sin θ, although the nature of this second-order dependence differs from one data set to the other (see the electronic supplement). This is not terribly surprising, as Bowering and Huber used completely different experimental configurations. It may be that a more general evaluation of second-order trends would be most productively elucidated by way of accurate numerical simulations using carefully controlled input conditions and appropriately selected measurements. The time and effort involved in performing such simulations is likely much less than in the parallel experimental work.

[46] In our experiments we measured the dimensional quantities V_w and t_s, the landslide volume per unit width and the duration of landslide motion, respectively. If we are interested in applying equations (22) and (25) for prognostic purposes (assessing hazards associated with a hypothetical mass flow), V_w is not known in advance and must be estimated. Geotechnical arguments may be used to estimate the probable volume of a slope failure, say, and flow width can be constrained by considering the topography of the flow path. Other information one could apply in trying to estimate V_w include empirical scaling relations between flow volume and the cross-sectional area of the subaerial channel that conveys the flow [*Iverson et al.*, 1998], and of course geological evidence bearing on the behavior of past flows. The duration of submerged landslide motion, t_s, is also unknown in advance, but equation (30), along with bathymetric data and geologically based estimates of landslide length, provides a starting point for estimating t_s.

[47] Alternatively, for purposes of assessing hazards, one may wish to focus not on estimating V_w and t_s separately but rather to put bounds on the rate of displacement of water. The rationale for doing this comes from rewriting the dimensionless quantity V_w^*/t_s^* as $V_w^*/t_s^* = (V_w/t_s)/(h\sqrt{gh})$. Say that a mass flow with total volume V_w per unit width enters a water body over some finite period of time t_f. The flux per unit width may be denoted $q_w(t)$, and its maximum value $q_{\max}$ must be an upper bound on the rate of displacement of water. The corresponding upper bound on the dimensionless rate of displacement V_w^*/t_s^* is thus $q_{\max}/h\sqrt{gh}$. This approach to bounding V_w^*/t_s^* may be particularly relevant if the mass flow of interest is a debris flow, in which case there may well be either historical or paleohydraulic evidence to help place bounds on probable values of $q_{\max}$.

[48] However one chooses to parameterize the mass flow that generates the tsunami, the near-field characteristics of that wave suffice to provide a proxy tsunami source that can be used as an initial condition in a wave propagation model to calculate far-field effects. Real water bodies are, of course, three-dimensional, and the near-field tsunami source also establishes the appropriate wave radiation pattern and directional energy propagation into the far field.

7.1. Application to Waves Caused by Geophysical Mass Flows

[49] We have identified three hydrodynamically distinct regions (the splash zone, the near field, and the far field) associated with the entry of a mass flow into a body of water and showed that wave amplitude in the near field is to first order a simple function of t_s^*/V_w^*, a nondimensional measure of the wave maker travel time. From the perspective of hazards assessment, one must determine in which region a particular site lies. If a site lies within the probable splash zone, then one must turn to physical scale models [e.g., *Pugh and Harris*, 1982; *Fritz et al.*, 2001] or to numerical models that fully account for coupling between solid and fluid motion (although as stated previously, it is unclear that models developed to date accurately represent mass flow dynamics). For mass flows entering relatively small, roughly equidimensional alpine lakes [e.g., *Evans*, 1989], it may be that the entire lake basin lies within the splash zone. It is hard to state this with great certainty because of the lack of data on deposit geometry. Typically, field investigators have estimated after the fact the volume of source rock and the wave run-up, but have not collected bathymetric data bearing on deposit dimensions (from which one could estimate the size of the splash zone, as the two are of comparable size).

[50] For sites within the near field, our results can be coupled with considerations of wave runup [e.g., *Synolakis*, 1987]. For sites within the far field, the same sort of wave run-up considerations may be applied after our results have been used as input to numerical wave propagation models that fully account for dispersive effects, bathymetric refraction, and wave front spreading.

[51] We believe that particular attention needs to be paid to potential hazards associated with debris flow-generated tsunamis, especially in places such as the Cascade Range of the northwestern United States, where lahars (volcanogenic debris flows) of exceptionally large volume, as much as several cubic kilometers, may originate on the flanks of stratovolcanoes [e.g., *Scott et al.*, 1995; *Iverson et al.*, 1998]. Such lahars, with recurrence intervals in the range of several hundred years to as much as a thousand years, pose hazards of low probability but extreme consequences. For example, very large lahars that originated at Mount

Rainier during postglacial times inundated areas around the Puget Sound that are now densely populated [*Scott et al.*, 1995; *Scott and Vallance*, 1995]. Those lahars moved along river valleys that in some cases are now dammed for flood control and electricity generation. Thus any assessment of hazards posed by future lahars needs to incorporate some understanding of what happens when a lahar enters a lake or reservoir. Recent hazards assessment studies done for Mount Rainier and other Cascade volcanoes have dealt with the issue of lahar entry into lakes in a heuristic fashion, for example, by employing the argument that a lahar would be "contained" within any reservoir whose volume exceeded that of the lahar itself [e.g., *Scott and Vallance*, 1995; *Walder et al.*, 1999]. Clearly a better approach is required, one based on an understanding of the actual physics, including water wave generation, propagation, and run-up on shores and structures. The scaling relations developed above can serve a key role in this endeavor by providing most of the information needed to specify the wave source.

[52] We consider next several cases of water bodies much longer than they are wide and for which all three regions (the splash zone, the near field, and the far field) may be identified. We made use of equations (22), (25), and (30) to make after the fact "predictions" of near-field wave characteristics.

7.2. Lituya Bay, Alaska

[53] The best characterized landslide-generated wave in Lituya Bay occurred 9 July 1958 [*Miller*, 1960]. The wave was apparently generated by a rockfall of volume about 3×10^7 m^3 near the head of the T-shaped bay. Water splashed to a height of about 520 m above sea level (asl). The splash has been successfully simulated in a physical scale model [*Fritz et al.*, 2001]. For our purposes, we note that the water displaced by the landslide wound up being displaced "around the bend" in the T-shaped bay and out toward the open ocean. An eyewitness quoted by *Miller* [1960, p. 57] estimated that at a distance of about 2.5 km from the head of the bay, the wave extended from shore to shore with a height of about 30 m. We now assess whether this wave amplitude is generally consistent with our scaling results. Taking $V = 3 \times 10^7$ m^3, $W = 2.5$ km (the approximate width of the bay in the presumed near field), and $h = 150$ m (the approximate mean depth at 2.5 km from the head of the bay), we find $V_w^* = 0.53$. To estimate t_s^*, we use Equation (30) with $L = 1350$ m, the width of the "top" of the T-shaped bay at the point where the landslide entered, and a local depth $h = 122$ m [*Fritz et al.*, 2001, Figure 3]. We then estimate from Equation (30) that $t_s^* \approx 15$ and from Equation (25) that $[x]$ (based on the local depth) is about 1800 m. Thus the transition from near field to far field would have been at a distance of about 5 km from the head of the bay, so the observer's estimate for wave height at 2.5 km from the head of the bay therefore applies to the near field. We further calculate $t_s^*/V_w^* \approx 28$, so using equation (22) with $h = 150$ m yields a predicted near-field wave height of about 20 m. Given the eyewitness' distance from the event and the various approximations involved in our estimate, the prediction is in reasonable agreement with observation.

7.3. Loenvann, Norway

[54] Destructive waves caused by landslides into this lake have occurred repeatedly [*Jørstad*, 1968]. We consider here the event of 13 September 1936, when a rockslide of volume about 10^6 m^3 entered the lake on the west bank about 2 km from its southern end. The total length of the lake is about 8 km. The part of the lake to the north of the slide area has a width of about 1 km, a maximum depth of 132 m, and an average depth of about 70 m. The part to the south is much narrower (about 300 m) and shallower (commonly about 15 to 25 m). We take $V = 5 \times 10^5$ m^3, that is, we assume half the displaced water went north and half went south. We estimate $t_s^* \approx 16.4$ from equation (30) using $L = 400$ m, the approximate width of the lake where the landslide entered, and a *local* depth $h = 30$ m. For the lake to the north of the landslide, we then calculate $V_w^* \approx 0.10$, $t_s^*/V_w^* \approx 160$, $[x] \approx 1150$ m; the near-field/far-field transition is therefore at a distance of about 3.5 km from the source, and the near-field wave height predicted from equation (22) is about 3 m. Measurements indicate wave heights typically 2 to 5 m within the putative near-field zone [*Jørstad*, 1968, Figure 9]. For the southern part of the lake, we calculate (with $W = 300$ m and $h = 20$ m) $V_w^* \approx 4.2$, $t_s^*/V_w^* \approx 3.9$, and $[x] \approx 330$ m; the near-field/far-field transition is therefore at a distance of about 1 km from the source. We predict near-field wave amplitude of about 11 m. For comparison, measurements indicate wave heights 13 to 23 m within about 500 m of the probable splash zone. We conclude that predictions based on our experimentally based scaling relation do a reasonable job.

7.4. Swift Reservoir, Washington

[55] The 18 May 1980 eruption of Mount St. Helens triggered several lahars on the south side of the volcano [*Pierson*, 1985], including some that entered Swift Reservoir, which is operated for hydropower generation. Nearly all the lahar volume entered the reservoir at a point about 12 km distant from the dam. A gauge at the dam recorded a complex wave train, with the amplitude of the leading wave being about 0.4 m, and a net rise in stage of about 0.8 m over a period of about 2 hours. A reconstructed lahar hydrograph suggests a peak flow of about 7500 m^3/s. The reservoir width W is about 1 to 1.5 km, so we estimate $q_{\max}$ to be in the range 5 to 7.5 m^2/s, and using the average depth h of 61 m, we find t_s^*/V_w^* to be in the range 200 to 300, and thus a predicted near-field wave height of about 1.5 to 2 m. Note that we have not separately estimated t_s^* here.

[56] Unfortunately there are no data for comparing to the predicted wave heights. (Swift Reservoir was in the "red zone" of extreme danger during the period leading up to the eruption of Mount St. Helens, and all people were excluded from the area.) If we assume $t_s^* \approx 10$, then $[x] \approx 10h \approx 600$ m and we would expect the transition to far-field behavior to have been at a distance of about 1.8 km beyond the splash zone. It seems clear that the gauge record at the dam represents far-field wave propagation.

8. Conclusions

[57] We have investigated water waves generated by subaerial mass flows, with special attention to wave properties in the near field, by which we mean the region just beyond where the landslide stops, say, at a distance on the order of one wavelength, close enough to the source that the effect of dispersion on wave shape is negligible. In the near

field so defined, the water displaced by the mass flow propagates as a distinct wave "hump" free of the complex splashing motions that occur near the shore. Scaling analysis of the equations of motion indicates that the quantities controlling near-field wave properties may be chosen as nondimensional landslide volume per unit width, V_w^*, nondimensional submerged time of motion, t_s^*, and nondimensional vertical impact speed, Fr sin θ. Our experimental results, and those of *Bowering* [1970] and *Huber* [1980], can to first order be cast in the simple form $\tilde{\eta} = A(t_s^*/V_w^*)^{-b}$, where $\tilde{\eta}$ is wave amplitude as a fraction of water depth and A and b are empirically determined constants. This expression works remarkably well over at least two orders of magnitude variation in t_s^*/V_w^*, up to the limit of breaking waves, for both rigid and deformable wave makers. Our data show no clear second-order dependence of wave amplitude on Fr sin θ. The nondimensional time of motion t_s^* can be expressed to a good approximation as const. $(L/h)^{0.5}$, where L is landslide length. The experimentally based scaling relation does a good job of "predicting" near-field wave amplitude for several historical events.

Appendix A: Relative Timescales

[58] Wave maker problems generally involve two timescales: one (t_s) characterizes the wave maker time of motion, the other (t_w) characterizes the time for deep-water waves to cross the wave generation zone [*Hammack*, 1973; *Iwasaki*, 1982; *Watts*, 1997, 1998]. We implicitly assumed in the scaling analyses of the main text that $t_s < t_w$ and that t_s would be the appropriate choice of timescale to nondimensionalize the Euler equations. Here we provide some justification of this choice.

[59] Consider first the initial velocity case, with a block sliding down a ramp sloping at angle θ into a constant depth tank. Motion is assumed to be resisted by friction between the block and the bed, with friction angle ϕ. The block moves down the ramp with a net acceleration $\alpha = g \sin\theta(1 - \tan\phi/\tan\theta)$ and reaches the bottom after a time

$$t_r = \frac{-U_0 + \left(U_0^2 + 2\alpha h/\sin\theta\right)^{1/2}}{\alpha} \tag{A1}$$

The block then moves along the horizontal bed under a deceleration $-g \tan\phi$ and comes to rest after an additional time

$$t_b = \frac{\left(U_0^2 + 2\alpha h/\sin\theta\right)^{1/2}\cos\theta}{g\tan\phi} \tag{A2}$$

The total travel time t_s is $t_r + t_b$. To compute t_w, we note that the local long-wave celerity is $\sqrt{gh(x)}$, and calculate the wave travel time for each segment (ramp and constant depth channel) separately. The desired result, after some algebra, is

$$\frac{t_s}{t_w} \approx \frac{\dfrac{-\mathrm{Fr} + \xi(\mathrm{Fr},\alpha)}{\alpha/g} + \dfrac{\xi(\mathrm{Fr},\alpha)\cos\theta}{\tan\phi}}{\dfrac{2}{\tan\theta} + \dfrac{\xi(\mathrm{Fr},\alpha)\cos^2\theta}{2\tan\phi}} \tag{A3}$$

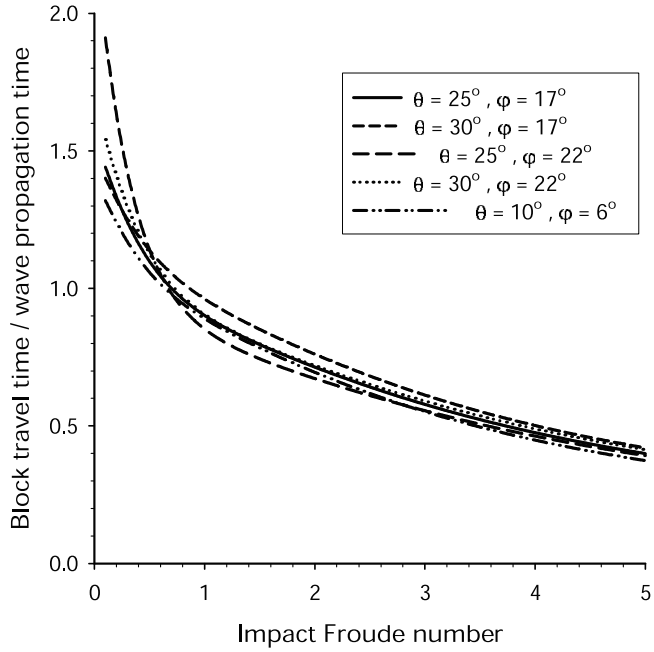

Figure A1. Ratio of wave maker travel time (t_s) to time of long-wave propagation across the wave generation zone (t_w), as a function of the impact Froude number, for an idealized initial velocity configuration; θ is bed slope, and ϕ is friction angle.

where $\xi(\mathrm{Fr}, \alpha) = \mathrm{Fr}^2 + 2\alpha/g \sin\theta$. Figure A1 shows the variation of t_s/t_w as a function of Fr for representative values of θ and ϕ. The plots for $\phi = 17°$ should be representative of our block landslide experiments [cf. *Watts*, 1997, 1998]; the plots for $\phi = 22°$ are representative of the gravel flows of *Huber* [1980]; and the plot for $\theta = 10°$, $\phi = 6°$ represents a debris flow moving down a moderately steep channel, with the very low friction coefficient crudely mimicking the fact that debris flows are largely fluidized [*Iverson*, 1997; *Iverson and Vallance*, 2001]. We conclude that $t_s/t_w < 1$ as long as Fr is greater than about 0.8. All of our initial velocity experiments were conducted with Fr > 1, so the choice of t_s to scale the Euler equations is reasonable.

[60] Now consider the release-from-shore case, assuming, as in our experiments with blocks, that the wave maker essentially slams into the bottom and then stops. The width of the wave generation zone is then $h/\tan\theta$ and $t_w \approx 2\sqrt{h/g}/\tan\theta$ [*Iwasaki*, 1982, p. 252]. Suppose for simplicity that motion is resisted solely by friction between the block and the bed, with friction angle ϕ. The block moves down the ramp with a net acceleration α and slams into the bottom after a time $t_s = \sqrt{2h/\alpha \sin\theta}$. Thus

$$\frac{t_s}{t_w} \approx \left(\frac{g\sin\theta}{2\alpha\cos^2\theta}\right)^{1/2} \tag{A4}$$

Figure A2 shows the behavior of this function for a range of θ and ϕ. Our experiments, with $\theta = 30°$ and $\phi \approx 17°$, correspond to $t_s/t_w \approx 1$. Thus either t_s or t_w would appear to be reasonable choices for scaling the Euler equations.

[61] Considering Figure A1 again, we see that for landslides moving sufficiently slowly or entering sufficient deep

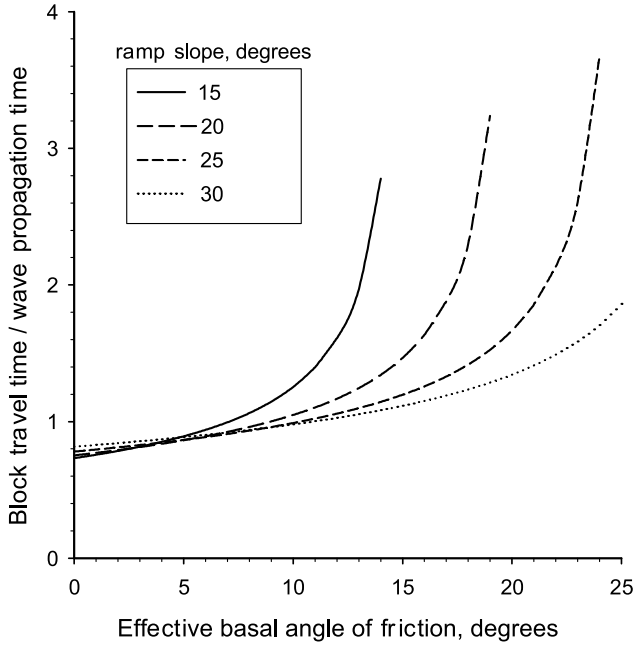

Figure A2. Ratio of wave maker travel time (t_s) to time of long-wave propagation across the wave generation zone (t_w), as a function of the impact Froude number, for an idealized release-from-shore configuration; θ is bed slope, and ϕ is friction angle.

water, t_w would probably be the appropriate choice for scaling the Euler equations. It can be shown (but we do not present details here) that scaling time by t_w introduces another nondimensional grouping into the scaled Euler equations, namely, t_s/t_w = Ha, the so-called Hammack number of *Watts* [1997, 1998]. For various reasons, it is difficult to design laboratory-scale initial velocity experiments for which $t_s/t_w > 1$.

Appendix B: Impulsive Effects

[62] In the block-motion analysis of the main text, we scaled the submerged speed of the block by U_0, the block speed at the moment of impact with the water. The impact forces integrated over the short but finite time of impact constitute an impulsive resistance to block motion, so in general the block will slow down as it enters the water, and thus submerged motion should really be scaled by $\tilde{U}(<U_0)$, the speed after application of the impulse. We can make a rough estimate of the impulsive effect by considering impact of a block with water at normal incidence. We estimate the impulse applied per unit width, I, as [cf. *Batchelor*, 1967, pp. 471–474]

$$I = \text{const}\,\rho T^2 U_0 \tag{B1}$$

where T is block thickness and the constant is $O(1)$. This impulse reduces the block's momentum P, which at impact is (per unit width)

$$P = \text{const}\,\gamma\rho T L U_0 \tag{B2}$$

and again the constant is $O(1)$. Thus

$$\frac{I}{P} \approx \left(\frac{T}{\gamma L}\right) \tag{B3}$$

to within an $O(1)$ constant. This almost certainly overestimates the impulsive effect in our experiments, which used blocks with a tapered front and an incidence angle much less than 90°. As long as $I/P \ll 1$, there is little change in block speed at impact and we are justified in using U as the scaling quantity. In our initial velocity experiments, $\gamma = 2.9$, $T/L < 0.3$, so I/P is in fact $\ll 1$. The same should hold for actual geophysical mass flows, for which $\gamma \approx 2$ and $T/L \ll 1$. Thus we expect that impulsive slowing will only be important for laboratory cases involving, say, short, low-density blocks. This probably describes the initial experimental runs of *Bowering* [1970], as he used a weighted box with $T/L \approx 0.4$ and specific gravities in some cases <1. We did not consider any of these data for comparison to our own.

[63] We should state as a caveat that the argument above strictly applies only to rigid blocks. Actual geophysical mass flows are not rigid and will deform as they enter a body of water. One might expect to see, say, some thickening at the snout of the flow, and indeed this has been seen in the laboratory with gravel-sized particles [*Fritz et al.*, 2001]. Just how such flow front thickening affects wave generation remains uncertain.

Appendix C: Assessment of Effects of Viscosity and Surface Tension in the Experiments

[64] For our laboratory experiments to be reasonable simulations of actual landslides entering water, forces associated with both viscosity and surface tension must be negligible. We consider first viscous forces. If the scaling analysis of section 2 were done on the full Navier-Stokes equations instead of the Euler equations, we would find that viscous forces scale with a Reynolds number $\text{Re} \approx \rho_w L\sqrt{(gh)}/\mu$ [cf. *Watts*, 1997, p. 39]. For our experiments, we find $\text{Re} \approx 10^5 - 10^6$ and conclude that a very thin boundary layer must rapidly develop as the block submerges. For actual landslides entering lakes, the value of Re would almost certainly be even greater. The skin friction associated with the boundary layer can be parameterized by a drag coefficient C_f commonly of order $Re^{-1/2}$ [cf. *Schlichting*, 1979], and thus negligible compared to the drag coefficient C_d associated with form drag (section 6), which is typically order unity. We conclude that viscous forces play a negligible role in wave maker dynamics at both laboratory scale and natural scale. A similar argument can be made about viscous damping of the water waves generated (owing to bottom drag and, in the flume, side drag) over the typical length scale of the near field [cf. *Keulegan*, 1948; *Naheer*, 1978].

[65] Surface tension has a negligible effect on wave propagation for wavelengths greater than about 20 mm [e.g., *Dean and Dalrymple*, 1991; *Johnson*, 1997] and is certainly negligible for all our experimentally generated waves. Surface tension almost certainly plays a role in the splash zone, for example, in droplet formation, for all plausible wave maker sizes, whether in the laboratory or

in nature. Any such effects are implicit in the black-box treatment of the wave generation process. Indeed, we conclude that overall, the laboratory experiments properly scale diverse splash zone phenomena.

Appendix D: Reanalysis of Data From Huber and Bowering

[66] We reanalyzed data from the theses of *Bowering* [1970] and *Huber* [1980] in the context of our scaling analysis, which highlighted the importance of the rate of water displacement by the landslide mass. Neither Bowering nor Huber provided explicit data about the travel time t_s of the wave makers, but it was still possible to make plausible estimates of t_s for some of their experiments, as discussed next. *Huber* [1980] released gravel flows with mass M as much as 50 kg down a sloping ramp into a constant depth tank of water. The initially compact gravel mass invariably elongated and thinned greatly by the time it reached the water tank, which was 30.4 m long, with a width W of 0.5 m and water depth h ranging from 0.12 to 0.36 m. Huber systematically varied slope θ and impact speed U_0 and recorded maximum wave amplitude at several locations along the tank, but reported no measurements of submerged wave maker travel time. Huber did a total of 348 experiments with a constant depth tank, with ramp slopes ranging from 28° to 60°. We reanalyzed data for all these experiments, but for comparison to our own data, we considered only experiments with bed slopes ranging from 28° to 35° (a total of 149 experiments). For greater slopes, gravel flows would be very thin and poorly characterized by a continuum approximation [cf. *Savage and Hutter*, 1989]. We proceeded by making certain plausible assumptions. The displaced water volume V_w per unit width can be bounded by

$$\frac{M}{W\rho_g} \le V_w \le \frac{M}{W\rho_g\left(1-\tilde{\phi}\right)} \tag{D1}$$

where ρ_g is the grain density, taken as 2.67×10^3 kg/m^3, and $\tilde{\phi}$ is the bulk porosity of the gravel flow. The lower bound applies if the flow is so permeable that water passes freely through the gravel; the upper bound applies if the permeability is so low that the ambient water is simply pushed aside. Huber's gravels were coarse enough (median grain size about 20 mm) that they should have been highly permeable. However, if water passed freely through the pores, then flow speed in the pores would have been $O(U_0/\phi)$, or commonly several m/s. Such high flow speeds would correspond to very large pore Reynolds numbers (>ca. 10^4) and distinctly non-Darcian flow [e.g., *Dullien*, 1979]. Moreover, flow paths and hydraulic head gradients are unknown a priori. Given all the uncertainties involved, we simply pick the lower bound in equation (D1) but recognize that V_w may be underestimated by as much as, say, 30%. We then estimated t_s by assuming that gravel motion was resisted solely by Coulomb frictional forces at the bed and calculating the travel time first along the ramp, then along the horizontal bed, by the method described in Appendix A. This method of estimating t_s obviously has its drawbacks, as the granular flow mechanics are dealt with very simplistically. Longitudinal stress transmission [*Savage and Hutter*, 1989] has been ignored, as have the centripetal forces associated with change in slope [*Iverson and Denlinger*, 2001]. Alternative methods involving, say, the granular flow model of *Iverson and Denlinger* [2001] would likely be better, but would still suffer from our inability to make direct comparisons to data. The probable error in the estimated volumetric displacement rate V_w/t_s (and thus in V_w^*/t_s^*) will be quite large, say around 40%.

[67] We used Huber's wave amplitude data only for wave gauges placed at a distance x from the entry point equal to $5h$, which is of the same order as the typical wavelength measured at that point [cf. *Huber*, 1980, Table 10a] and also beyond the distal end of the associated deposit, i.e., beyond the splash zone [cf. *Huber*, 1980, Figure 14]. Thus $x = 5h$ can probably be considered near field in the terms defined in the main text. Huber's measurements at greater distances from the point of impact, starting at $x = 10h$ (his Tables 10b–10e), show effects of wave broadening associated with dispersion and cannot be considered near-field measurements.

[68] *Bowering* [1970] did two distinct sets of experiments. We disregarded his earliest experiments using fixed-volume boxes, as specific gravity varied from test to test and impulsive slowing was probably important in some tests. We considered only his later "modified box" experiments, involving an open-framework "sled" with a wedge-shaped cross section and an adjustable front face, behind which were placed solid weights. The "landslide" masses all had a specific gravity of 2.7, a width of 0.91 m, and were allowed to slide down a ramp consisting of closely spaced roller bearings into a 45 m long constant depth tank of water. Landslide thickness varied from 1/8 to 7/8 of the water depth. Bowering varied mass M but did not control impact speed and provided no information as to whether the blocks were arrested at the bottom of the slope or allowed to come to rest naturally. Neither do we know whether the sled began to decelerate as soon as it hit the water. We assumed that the sled did not travel beyond the bottom of the slope, an assumption consistent with what we observed in our release-from-shore experiments, and bounded t_s by $h/(U_0 \sin\theta) \le t_s \le 2h/(U_0 \sin\theta)$. The lower bound would apply if the sled did not decelerate at all before stopping abruptly at the base of the slope; the upper bound would apply if the sled slowed to rest just as it reached the bottom of the slope. We picked t_s as the mean of the two bounds, that is, $t_s = 1.5h/U \sin\theta$, and thus $t_s^* = 1.5/\mathrm{Fr} \sin\theta$. This is admittedly a very rough approximation. The probable error in V_w/t_s is difficult to estimate; we will use a figure of 35% but recognize that this is only a rough guess.

[69] We used Bowering's wave amplitude data only for a gauge placed at a distance x from the entry point equal to $11h$, comparable to the typical trough-to-trough wavelength of about $10h$ to $15h$ [cf. *Bowering*, 1970, Figure 39]. Thus $x = 11h$ is probably in the near field in the terms defined in the main text. We disregard Bowering's measurements with gauges at distances $x = 33h$ and $x = 58h$, which presumably cannot be considered near-field locations.

[70] We also examined experimental data presented by other investigators [e.g., *Law and Brebner*, 1968; *Das and Wiegel*, 1972; *Sander and Hutter*, 1992] but could not

extract sufficient information from their papers to recast their results in terms of our dimensionless variables.

Notation

A regression coefficient.
b regression coefficient.
B regression coefficient.
C_d hydrodynamic drag coefficient.
C_f skin friction coefficient.
C_m added mass coefficient.
C_s regression coefficient
Fr Froude number of landslide block at impact.
$\mathrm{Fr}_{\max}$ maximum landslide Froude number during submergence.
g acceleration due to gravity, m/s^2.
h water depth, m.
H height of landslide release relative to water surface, m.
I impulse per unit width applied to block entering water, kg/s.
L length of landslide block, m.
m regression coefficient.
M mass of landslide, kg.
n regression coefficient.
p dimensionless measure of water pressure.
p' water pressure, Pa.
P momentum per unit width of landslide entering water, kg/s.
q regression coefficient.
$q_{\max}$ maximum value of q_w, m^2/s.
q_w flux (discharge) of mass flow per unit width, m^2/s.
Q_w^* dimensionless measure of rate of water displacement per unit width by landslide.
r regression coefficient.
Re Reynolds number.
s dimensionless coordinate in direction of landslide movement.
s' coordinate in direction of landslide movement, m.
t dimensionless time.
t' time, s.
$[t]$ characteristic scale for time, s.
t_b portion of landslide travel time along base, s.
t_r portion of landslide travel time along ramp, s.
t_s characteristic time of submerged landslide motion, s.
t_w time for long waves to cross wave generation zone, s.
t_s^* dimensionless measure of time of submerged landslide motion.
T thickness of landslide block, m.
u dimensionless measure of water speed in direction of water propagation.
u' water speed in direction of water propagation, m/s.
U_0 landslide block speed just before impact with water, m/s.
$\tilde{U}$ landslide block speed just after impact with water, m/s.
$U_{\max}$ maximum landslide speed during submergence, m/s.
Ur Ursell parameter of wave.
V_w landslide volume per unit width normal to direction of wave propagation, m^2.
V_w^* dimensionless landslide volume per unit width normal to direction of wave propagation.
w dimensionless water speed in direction normal to undisturbed water surface.
w' water speed in direction normal to undisturbed water surface, m/s.
W width of landslide block in direction normal to block motion, m.
x dimensionless coordinate in direction of wave motion.
x' coordinate in direction of wave motion, m.
$[x]$ characteristic scale for coordinate length in direction of wave motion, m.
z dimensionless coordinate in direction normal to undisturbed water surface.
z' coordinate in direction normal to undisturbed water surface, m.
α characteristic landslide acceleration during submergence, m/s^2.
γ bulk specific gravity of landslide.
η $\eta'/[\eta]$, a dimensionless measure of wave amplitude.
η' wave amplitude, m.
$[\eta]$ characteristic measure of wave amplitude used in scaling analysis, m.
$\tilde{\eta}$ η'/h, wave amplitude as a fraction of water depth.
θ slope angle at shoreline.
λ characteristic measure of wavelength in the near field, m.
μ viscosity of water, Pa s.
ρ_w density of water, kg/m^3.
ρ_g grain density of landslide mass, kg/m^3.
τ_H elapsed time for landslide released at height H to reach water depth h, s.
τ_{sH} submerged part of τ_H, s.
τ_{ss} elapsed time for landslide released at shoreline to reach water depth h, s.
υ fitting parameter in block motion analysis.
ϕ friction angle.
ϕ porosity.
χ $= \sin\theta\,(1 - \tan\phi/\tan\theta)$.

[71] **Acknowledgments.** The flume for the initial velocity experiments was primarily built by T. Wellman. The release-from-shore experiments were done in the Geological Fluid Dynamics Laboratory, Department of Earth Sciences, University of Bristol, England. Joseph Walder thanks R.S.J. Sparks for an invitation to spend time in the department and J.C. Phillips for permission to use the Laboratory. J.W. Kamphuis (Queen's University, Kingston, Ontario, Canada) kindly provided a photocopy of the unpublished M.S. thesis of Bowering. Joseph Walder thanks the staff of the Observatorio Volcanológico de los Andes del Sur in Temuco, Chile, where he was resident while writing early drafts of this paper. Richard Iverson, Jonathan Nelson, Simon Day, and an anonymous referee carefully reviewed earlier versions of this paper. Mention of trade names is for identification purposes only and does not constitute endorsement by the U.S. Geological Survey.

References

Assier Rzadkiewicz, S., C. Mariotti, and P. Heinrich, Numerical simulation of submarine landslides and their hydraulic effects, *J. Waterw. Port Coastal Ocean Eng.*, *123*, 149–157, 1997.

Batchelor, G. K., *An Introduction to Fluid Dynamics*, 615 pp., Cambridge Univ. Press, New York, 1967.

Ben-Menahem, A., and M. Rosenman, Amplitude patterns of tsunami waves from submarine earthquakes, *J. Geophys. Res.*, *77*, 3097–3128, 1972.

Bowering, R. J., Landslide generated waves: a laboratory study, M.S. thesis, 155 pp., Queen's Univ., Kingston, Ont., Canada, 1970.

Cas, R. A. F., and J. V. Wright, *Volcanic Successions: Modern and Ancient*, 528 pp., Allen and Unwin, Concord, Mass., 1987.

Das, M. M., and R. L. Wiegel, Waves generated by horizontal motion of a wall, *J. Waterw. Harbors Coastal Eng. Div. Am. Soc. Civ. Eng.*, *98*, 49–65, 1972.

Dean, R. G., and R. A. Dalrymple, *Water Wave Mechanics for Engineers and Scientists*, 353 pp., World Sci., River Edge, N. J., 1991.

Denlinger, R. P., and R. M. Iverson, Flow of variably fluidized granular masses across three-dimensional terrain: 2. Numerical predictions and experimental tests, *J. Geophys. Res.*, *106*, 553–566, 2001.

Dullien, F. A. L., *Porous Media:Fluid Transport and Pore Structure*, 396 pp., Academic, San Diego, Calif., 1979.

Evans, S. G., The 1946 Mount Colonel Foster rock avalanche and associated displacement wave, Vancouver Island, British Columbia, *Can. Geotech. J.*, *26*, 447–452, 1989.

Freundt, A., The entrance of pyroclastic flows into the sea, *Eos Trans. AGU*, *82*(47), Fall Meet. Suppl., Abstract V12F-05, 2001.

Fritz, H. M., W. H. Hager, and H.-E. Minor, Lituya Bay case: rockslide impact and wave run-up, *Sci. Tsunami Hazards*, *19*, 3–22, 2001.

Gozali, S., and B. Hunt, Water waves generated by close landslides, *J. Hydraul. Res.*, *27*, 49–60, 1989.

Hammack, J. L., A note on tsunamis: Their generation and propagation in an ocean of uniform depth, *J. Fluid Mech.*, *60*, 769–799, 1973.

Heinrich, P., Nonlinear numerical model of landslide-generated water waves, *Int. J. Eng. Fluid Mech.*, *4*, 403–416, 1991.

Heinrich, P., Nonlinear water waves generated by submarine and aerial landslides, *J. Waterw. Port Coastal Ocean Eng.*, *118*, 249–266, 1992.

Huber, A., Schwallwellen in Seen aus Folge von Felsstürzen, *Mitt. VAW-ETH 47*, 222 pp., Eidg. Tech. Hochsch., Zürich, 1980.

Huber, A., Felsbewegungen und Uferabbrüche an Schweizer Seen, ihre Ursachen und Auswirkungen, *Eclogae Geol. Helv.*, *75*, 563–578, 1982.

Hunt, B., Water waves generated by distant landslides, *J. Hydraul. Res.*, *26*, 307–322, 1988.

Imamura, F., and E. C. Gica, Numerical model for tsunami generation due to subaqueous landslide along a coast, *J. Sci. Tsunami Hazards*, *14*, 13–28, 1996.

Imamura, F., and M. M. A. Imteaz, Long waves in two-layers: governing equations and numerical model, *J. Sci. Tsunami Hazards*, *13*, 2–24, 1995.

Iverson, R. M., The physics of debris flows, *Rev. Geophys.*, *35*, 25–296, 1997.

Iverson, R. M., and R. P. Denlinger, Flow of variably fluidized granular masses across three-dimensional terrain: 1. Coulomb mixture theory, *J. Geophys. Res.*, *106*, 537–552, 2001.

Iverson, R. M., and J. W. Vallance, New views of granular mass flows, *Geology*, *29*, 115–118, 2001.

Iverson, R. M., S. P. Schilling, and J. W. Vallance, Objective delineation of lahar-inundation hazard zones, *Geol. Soc. Am. Bull.*, *110*, 972–984, 1998.

Iwasaki, S., Experimental study of a tsunami generated by a horizontal motion of a sloping bottom, *Bull. Earthquake Res. Inst. Univ. Tokyo*, *57*, 239–262, 1982.

Iwasaki, S., The wave forms and directivity of a tsunami generated by an earthquake and a landslide, *Sci. Tsunami Hazards*, *15*, 23–40, 1997.

Jiang, L., and P. H. LeBlond, The coupling of a submarine slide and the waves which it generates, *J. Geophys. Res.*, *97*, 12,731–12,744, 1992.

Jiang, L., and P. H. LeBlond, Numerical modeling of an underwater Bingham plastic mudslide and the waves which it generates, *J. Geophys. Res.*, *98*, 10,303–10,317, 1993.

Jiang, L., and P. H. LeBlond, Three-dimensional modeling of tsunami generation due to a submarine landslide, *J. Phys. Oceanog.*, *24*, 559–572, 1994.

Jørstad, F. A., Waves generated by landslides in Norwegian fjords and lakes, *Norw. Geotech. Inst. Publ.*, *79*, 13–32, 1968.

Johnson, R. S., *A Modern Introduction to the Mathematical Theory of Water Waves*, 445 pp., Cambridge Univ. Press, New York, 1997.

Kamphuis, J. W., and R. J. Bowering, Impulse waves generated by landslides, *Proc. Coastal Eng. Conf.*, *11th*, 575–588, 1970.

Keulegan, G. H., Gradual damping of solitary waves, *J. Res. Natl. Bur. Stand.*, *40*, 487–498, 1948.

Kilburn, C. R. J., and S.-A. Sørensen, Runout lengths of sturzstroms: the control of initial conditions and fragment dynamics, *J. Geophys. Res.*, *103*, 17,877–17,884, 1998.

Law, L., and A. Brebner, On water waves generated by landslides, paper presented at Third Australasian Conference on Hydraulics and Fluid Mechanics, Inst. of Eng., Sydney, Australia, 25–28 Nov. 1968.

Lighthill, J., *Waves in Fluids*, 504 pp., Cambridge Univ. Press, New York, 1978.

Miller, D. J., Giant waves in Lituya Bay, Alaska, *U.S. Geol. Surv. Prof. Pap., 354-C*, 86 pp., 1960.

Mohrig, D., K. X. Whipple, M. Hondzo, C. Ellis, and G. Parker, Hydroplaning of subaqueous debris flows, *Geol. Soc. Am. Bull.*, *110*, 387–394, 1998.

Naheer, E., The damping of solitary waves, *J. Hydraul. Res.*, *16*, 235–249, 1978.

Noda, E., Water waves generated by landslides, *J. Waterw. Harbors Coastal Eng. Div. Am. Soc. Civ. Eng.*, *96*, 835–855, 1970.

Norem, H., J. Locat, and B. Schieldrop, An approach to the physics and the modelling of submarine landslides, *Mar. Geotech.*, *9*, 93–111, 1990.

Pierson, T. C., Initiation and flow behavior of the 980 Pine Creek and Muddy River lahars, Mount St. Helens, Washington, *Geol. Soc. Am. Bull.*, *96*, 1056–1069, 1985.

Plafker, G., and V. R. Eyzaguirre, Rock avalanches and wave at Chungar, Peru, in *Rockslides and Avalanches*, vol. 2, edited by B. Voight, pp. 269–279, Elsevier Sci., New York, 1979.

Pugh, C. A., and D. W. Harris, Prediction of landslide-generated water waves, paper presented at 14th International Congress on Large Dams, Int. Comm. on Large Dams, Rio de Janeiro, Argentina, 1982.

Raichlen, F., J. J. Lee, C. Petroff, and P. Watts, The generation of waves by a landslide: Skagway, Alaska case study, *Proc. Int. Conf. Coastal Eng.*, *25th*, 1293–1300, 1996.

Sander, J., and K. Hutter, Evolution of weakly non-linear shallow water waves generated by a moving boundary, *Acta Mech.*, *91*, 119–155, 1992.

Sander, J., and K. Hutter, Experimental and computational study of channelized water waves generated by a porous body, *Acta Mech.*, *115*, 133–149, 1996.

Savage, S. B., and K. Hutter, The motion of a finite mass of granular material down a rough incline, *J. Fluid Mech.*, *199*, 177–215, 1989.

Schlichting, H., *Boundary-Layer Theory*, 7th ed., 817 pp., McGraw-Hill, New York, 1979.

Scott, K. M., Precipitation-triggered debris-flow at Casita Volcano, Nicaragua: implications for mitigation strategies in volcanic and tectonically active steeplands, in *Debris-Flow Hazards Mitigation: Mechanics, Prediction, and Assessment (Proceedings of the 2nd International Conference on Debris-Flow Hazards Mitigation, Taipei, Taiwan, 16–18 August 2000)*, edited by G. F. Wieczorek and N. D. Naeser, pp. 3–13, A. A. Balkema, Brookfield, Vt., 2000.

Scott, K. M., and J. W. Vallance, Debris flow, debris avalanche, and flood hazards at and downstream from Mount Rainier, Washington, *U.S. Geol. Surv. Hydrol. Invest. Atlas 729*, 1995.

Scott, K. M., P. T. Pringle, and J. W. Vallance, Sedimentology, behavior, and hazards of debris flows at Mount Rainier, Washington, *U.S. Geol. Surv. Prof. Pap., 1547*, 56 pp., 1995.

Synolakis, C. E., The runup of solitary waves, *J. Fluid Mech.*, *185*, 523–545, 1987.

Tappin, D. R., T. Matsumoto, P. Watts, K. Satake, G. M. McMurtry, M. Matsuyama, Y. Lafoy, and Y. Tsuji, Offshore surveys identify sediment slump as likely cause of devastating Papua New Guinea tsunami 1998, *Eos Trans. AGU*, *80*, 329, 1999.

Tappin, D. R., P. Watts, G. M. McMurtry, Y. Lafoy, and T. Matsumoto, The Sissano, Papua New Guinea tsunami of July 1998—Offshore evidence on the source mechanism, *Mar. Geol.*, *175*, 1–23, 2001.

Villeneuve, M., and S. B. Savage, Nonlinear, dispersive, shallow-water waves developed by a moving bed, *J. Hydraul. Res.*, *31*, 249–266, 1993.

Walder, J. S., C. A. Gardner, R. M. Conrey, B. J. Fisher, and S. P. Schilling, Volcano hazards in the Mount Jefferson region, Oregon, *U.S. Geol. Surv. Open File Rep., 99-24*, 14 pp., 1999.

Watts, P., Water waves generated by underwater landslides, Ph.D. dissertation, 319 pp., Calif. Institute of Technol., Pasadena, 1997.

Watts, P., Wavemaker curves for tsunamis generated by underwater landslides, *J. Waterw. Port Coastal Ocean Eng.*, *124*, 127–137, 1998.

Watts, P., Tsunami features of solid block underwater landslides, *J. Waterw. Port Coastal Ocean Eng.*, *126*, 144–152, 2000.

Watts, P., and J. S. Walder, Evaluating tsunami hazards from debris flows, paper to be presented at the 3rd International Conference on Debris-Flow Hazards Mitigation, Swiss Fed. Inst. for For., Snow and Landscape Res., Davos, Switzerland, 10–12 Sept. 2003.

Whitham, G. B., *Linear and Nonlinear Waves*, 636 pp., Wiley-Interscience, New York, 1974.

K. Janssen and J. S. Walder, U.S. Geological Survey, Cascades Volcano Observatory, 1300 Southeast Cardinal Court, Building 10, Suite 100, Vancouver, WA 98683, USA. (jswalder@usgs.gov)

O. E. Sorensen, Department of Geological Engineering and Sciences, Michigan Technological University, Houghton, MI 49931, USA.

P. Watts, Applied Fluids Engineering, Inc., Private Mail Box 237, 5710 E. 7th Street, Long Beach, CA 90803, USA. (phil.watts@appliedfluids.com)